Influence of reactive gas flow ratio during sputter deposition of Mo-O-N thin films on their structure and properties

Thaddäa Rath

Leoben, September 2018

This work was carried out at the Department of Engineering Physics, Polytechnique de Montréal, Canada, in corporation with the Chair of Functional Materials and Materials Systems at the Department of Physical Metallurgy and Materials Testing, Montanuniversität Leoben, Austria

Declaration of Academic Honesty

I declare in lieu of oath, that I wrote this thesis and performed the associated research myself, using only literature cited in this volume.

City, Date of issue *Signature*

Acknowledgment

I would like to express my sincerest gratitude to Univ. Prof. Christian Mitterer, head of the Department of Physical Metallurgy and Materials Testing, not only for the professional supervision but also for the support and encouragement before and during my stay in Montréal. I really appreciate all the effort he put in me.

Secondly I would like to thank Professor Ludvik Martinu and Professor Jolanta Sapieha, director and co-director of the Functional Coating and Surface Engineering Laboratory (LarFIS) at the Department of Engineering Physics at Polytechnique Montréal, for the possibility of spending the time needed to do experiments in their laboratories. Both were very welcoming and provided interesting and helpful aspects throughout the creation of this work.

My gratitude also goes to Dr. mont. Robert Franz, who answered all of my questions from the distance and after I returned. I am thankful for all Skype meetings, professional support, guidance and patience.

For their help, instructive trainings and time for answering my questions repeatedly during my stay in Montréal I would like to say special thanks to Bill Baloukas, Ph.D., Etienne Bousser, Ph.D., Simon Loquai, Ph.D., Jacques Lengaigne, MSc, Thomas Schmitt, Ph.D., Jincheng Qian, Ph.D. and Sacha Woodward-Gagné. Also, I would like to thank the entire LaRFIS group for very interesting Fridays lunch meetings and intellectual coffee breaks. I felt included from the start and it was a lot of fun working in this team.

I am grateful for my family and their never ending confidence in me. I could always trust in their mental and financial support. Furthermore I would like to thank my friends, who understand the principle of 'A sorrow shared is half a sorrow'. With that in mind, a special thanks goes to my study partner DI Sabine Bodner. Without all of them, studying would have been a lot harder.

Content

1 Introduction

Materials that are optically transparent and electrically conductive at the same time are an essential component in opto-electronic applications, such as flat panel displays, touchscreens, solar cells or smart windows. Most of the materials showing these typically contradictory properties are doped oxidic compounds, so-called transparent conductive oxides, with the most frequent being Sn-doped In_2O_3 (ITO) [1–4]. However, the material costs of In are increasing as the resources are limited and the manufacturing process can be quite complicated. ITO films also show a brittle fracture behaviour, which creates difficulties in its use in future flexible devices [5]. Researchers are therefore constantly looking for alternatives. Such alternative materials include Al- or Ga-doped ZnO and F-doped SnO_2 [2, 6]. But also nano-structured metals, such as Ag nanowires or ultra-thin films and single walled carbon nanotubes are considered as substitutes for ITO [7].

Transition metal oxynitrides (Me-O-N), with metals such as W, Ti, Ce, Cr, Hf, V, Ta, W or Mo, are known to combine sometimes contrary properties of oxides and nitrides [8–12]. With different O/N ratios it is possible to manipulate the microstructure, the bonding behaviour and oxidation state of the metal, which has an effect, especially, on the physical properties. The coloration, the photocatalytic behaviour, magnetoresistance effect and the emission wavelength of luminescent oxides is reported to be influenced by the addition of N [11]. Only little research has been conducted on the mechanical, optical and electrical properties of molybdenum oxynitride (Mo-O-N). The combination of the transparent MoO_3 and the conductive Mo_2N and thereby the possibility of Mo-O-N being an alternative to ITO is the incentive of this thesis.

Therefore, films of different N and O content, including pure Mo as a reference, were deposited to investigate the influence of N on the microstructure and the mechanical, optical and electrical properties. Using reactive magnetron sputtering, it was possible to manipulate the O/N ratio during the deposition by varying the reactive gas flow rates. Series of different thicknesses were deposited to discuss the possible effect of reduced thicknesses on the opto-electronic properties. The microstructure and chemical composition of specific samples was analysed using elastic recoil detection analysis (ERDA), X-ray photoelectron spectroscopy (XPS), electron dispersive X-ray spectroscopy (EDX), scanning electron microscopy (SEM) and X-ray diffraction (XRD). The mechanical properties were analysed by nanoindentation and micro-scratch testing. Transmission, reflexion, absorption, refractive index, extinction coefficient and energy band gap were determined using spectroscopic photo- and ellipsometry and the electrical resistivity was measured by a four point probe.

2 Theoretical Background

2.1 Molybdenum Oxynitrides

With an atomic number of 42, Mo is a transition metal of the Group VI in the periodic table. Showing a high melting point of 2610 °C and low coefficient of thermal expansion, it is categorised as refractory metal and it is one of the trace elements, essential for the growth of living organisms [13, 14]. The first industrial use was as additive in steel production, which is still the highest consumption of Mo worldwide [13].

Transition metals typically have more than one incomplete outer shell, which allows the formation of oxides with different oxidation states. For Mo the most stable oxidation states are Mo^{4+} and Mo^{6+} with the corresponding oxide phases being MoO_2 and MoO_3 [15, 16]. MoO_2 is an opaque material with a low electric resistivity, whereas MoO_3 shows transparent and insulating properties [17, 18]. The latter is also considered to be an electro- and photochromic material [19, 20]. Applications for MoO_3 are in the photovoltaic [21], photocatalytic [22] and gas sensing industry [23].

There are two stable phases of MoN_x, namely Mo_2N and MoN. Due to a combination of metallic, covalent and ionic bonding, they show a metal-like electrical behaviour and mechanical properties comparable to ceramics [24, 25]. MoN_x coatings can be used as Cu diffusion barriers in electronic devices [26–28], as hard protective coatings [29, 30], as catalysts for a CO_x-free H production [31] and are also suggested as superconductors [32, 33].

O and N show, due to the neighbouring position in the periodic table, similarities in ionic radius, coordination number and electronegativity, which makes them suitable substitutes for each other. However, with a different polarisability, bonding energy and electron affinity, the properties of the resulting Me-O-N may vary significantly with different N/O ratio [11]. The influence of N on MoO_x is a reduction of the band gap and a change in the oxidation state of the component transition metal, in this case Mo. It is therefore possible to manipulate the coloration, the tribological properties are enhanced and the photocatalytic activity is shifted towards the visible range [10, 11, 34, 35]. Current and suggested applications for Mo-O-N are the use as photo-catalyst for water splitting and degradation of organic molecules [9, 11, 12, 31, 36], anodes for lithium batteries [37], diffusion barriers in electronics [38] and as back contacts for solar cells [39].

2.2 Synthesis

2.2.1 DC Reactive Magnetron Sputter Deposition

Sputter deposition is a physical vapour deposition (PVD) technique, where the impact of gaseous ions on the surface of a source material (target) causes the ejection of atoms. The sputtered atoms can then condense on the surface of a provided substrate and form a continuous film as schematically shown in Figure 2.1.

For this procedure a vacuum chamber with an introduced heavy inert gas, typically Ar, is necessary to form a plasma. By applying a voltage, the ionised atoms in the gas are accelerated to the target (the cathode). These impingements cause the emission of secondary electrons, which are then accelerated to the anode and may collide with the gas atoms in the chamber, as can be seen in Figure 2.1. This results in the formation of new ions and free electrons and ultimately in maintaining the plasma [40–42]. In order to sputter an atom from the target surface, an impact with a sufficient energy is necessary to provoke a collision cascade in the near-surface area. An energetic hit from below the surface is essential to eject a surface atom out of the matrix [41, 42]. Preferably this atom will then directly approach the substrate to contribute to film growth and not be deflected by other particles in the chamber. This is relevant for the evolution of the microstructure and may affect the properties of the thin film.

The amount of target atoms that are sputtered from the surface by one incident ion can be expressed as sputter yield [41, 42]. It is influenced by a number of factors, such as the energy of the incident particle, the condition of the target surface or the angle of incidence [41]. The amount of target atoms that are sputtered per unit of time is the so-called sputter rate and is manipulated by the number of incident ions. In order to have a more efficient sputter rate, magnetron sputter deposition was developed in the 1980s. Due to the externally applied magnetic field, the electrons are deflected from their direct path to the anode and are trapped in the vicinity of the target surface. The result is a more efficient ionisation of the background gas [40–42]. With the available higher number of ions, an enhanced sputter erosion of the target material is achieved.

Another advantage of this setup is that a lower background gas pressure is required. Hence, less particles are present in the discharge and the probability of gas phase collisions is decreased. This leads to incident ions with higher energies, less scattering of the sputtered atoms and therefore a higher deposition rate [40, 41]. However, this implementation consequences the formation of the so-called erosion tracks. Depending on the magnetic field lines, i.e. the geometry of the target and the position of the magnets,

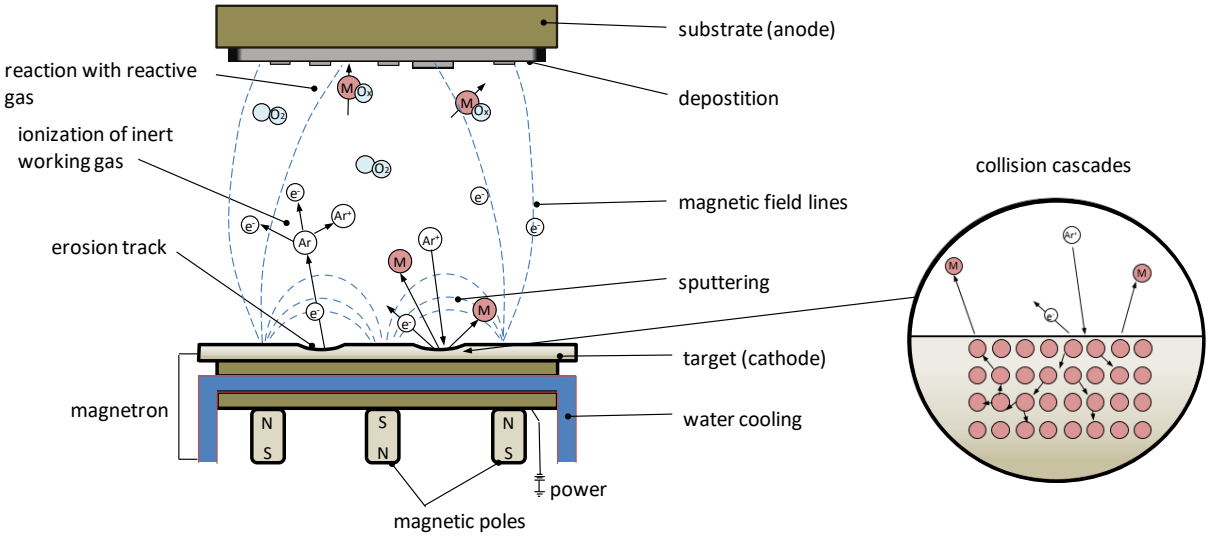

Figure 2.1: Schematic illustration of the processes occurring during reactive magnetron sputter deposition (after [43, 44]).

the erosion tracks can be rather concentrated or spread over a larger area of the target [40, 41, 45]. With time a groove is formed in the erosion track, which affects the sputter behaviour and alters the sputter rate and, ultimately, limits the lifetime of the target.

In conventional magnetron sputter deposition the target is powered by a DC voltage, which is the least expensive way of powering, yet it is limited to conductive targets [40–42]. Nevertheless it is possible to synthesise compound films by adding a reactive gas to the process chamber. The stoichiometry of the reaction product between the target atoms and the reactive gas atoms and/or molecules can be controlled by the gas partial pressure. This means with a low partial pressure of the reactive gas it is possible to form a metallic film with the reactive element as a dopant [42]. In most cases, however, the gas reacts not only with the sputtered target atoms, but with the target surface as well. As a result, a compound layer with a higher bonding energy than the pure metal is formed and the sputter yield and thereby the deposition rate are typically decreased [40, 41]. This phenomenon is called target poisoning.

In a sputter deposition system with DC powering and the formation of an insulating layer on the target, there is a greater risk of undesirable charge build-up and arcing [40]. The damage induced by arcing is a locally concentrated melting of the target, which can produce films of inferior quality. However, there are relatively simple methods to prevent the formation of an arc at the target surface. One such prevention is turning off the power for a few micro-seconds at a critical point of low voltage and high current by using an arc suppression unit [40].

The usage of a metallic target provides further advantages in addition to tailoring the

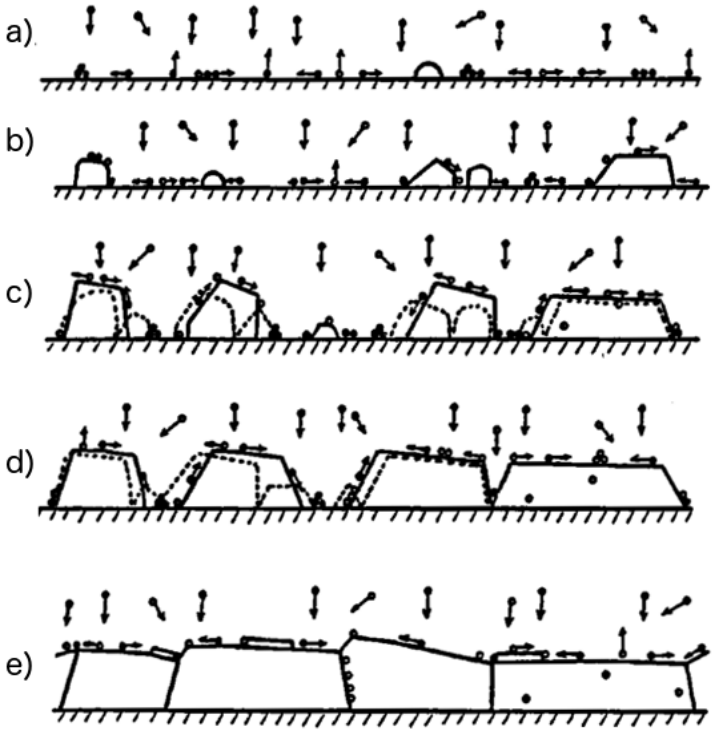

Figure 2.2: Schematic illustration of the processes during a) nucleation, b) island formation, c) island coalescence, d) continuous film formation and e) film growth [48].

stoichiometry of a compound. The manufacturing of a metallic target is accomplished by casting under protective atmosphere or via powder metallurgy [42, 45]. This makes metallic targets more cost-effective than non-metallic targets. The latter typically need to be sintered, which is more expensive and time consuming. Further, higher purities of up to 99.99 % can be achieved for metallic targets, whereas the purity of compound targets is usually below 99.9 % [42].

2.2.2 Thin Film Growth

As the sputtered atoms approach the substrate, the first step of film growth is the nucleation on the substrate surface. The loosely bonded adatoms move along the surface to either rest at a position of lower energy, including steps or cracks, or once again evaporate from the surface [46, 47]. The different stages of film growth, in this case island growth, starting at nucleation over coalescence of islands to a continuous film, are depicted in Figure 2.2.

Such low energetic locations might also be already existing nuclei and thereby the starting points of the formation of individual islands of the coating material. At low temperatures

and on an amorphous substrate, the nuclei have random orientation, as do the formed islands [48, 49]. Only as the islands grow larger and the substrate is heated to activate diffusion processes, neighbouring islands would coalesce to single or polycrystals with more favourable orientations. The coalescence is also a result of the desire to minimise the surface and interface energy [48, 49]. As the deposition process progresses, the islands continue to grow and combine at the expense of slower growing grains. Eventually the whole substrate surface is covered and a continuous film is formed.

The concept of structure zone models

To describe the evolution of the microstructure during film growth, several influencing factors need to be considered including the substrate temperature and the presence of impurities or additional elements. The change due to an increase in substrate temperature is described in the structure zone model (SZM) first developed by Movchan and Demchishin, who analysed the microstructure of a number of coatings that were synthesised at different temperatures [50]. After many years of improvement by various scientists [47–49, 51], SZMs are still the basis for characterising the microstructure of coatings.

In general, it can be stated that the columnar structure observed in PVD-produced films arises from the deposition method. Since the direction of material flux is mainly restricted to the line of sight between target and substrate, the film growth occurs in this direction [48]. However, the basic SZM of elemental depositions, as can be seen in Figure 2.3, describes three zones within a range of the homologous temperature, T_s/T_m, where T_s is the substrate temperature and T_m is the melting point of the coating material [48, 49].

In Zone I, i.e. at low homologous temperatures ($T_s/T_m < 0.2$), narrow, fibre-like columns are formed. These often appear in bundles with a high concentration of defects, such as dislocations and porous grain boundaries [47, 49]. Diffusion controlled processes are limited due to the low temperatures, hence no grain coarsening or rearrangement occurs and the grains are randomly oriented.

At higher temperatures, neighbouring crystals start to interact with each other and faster growing orientations dominate the microstructure. Throughout the film thickness, the crystals develop from fine-dispersed at the substrate surface to a columnar structure with larger diameter in the top region of thick coatings. The resulting V-shaped grains can be defined as competitive growth texture, which is characteristic for Zone T [49].

Increasing the temperature even further ($T_s/T_m > 0.4$) leads to Zone II with distinct columns forming the structure. These columns proceed over the whole thickness of the coating with grain boundaries that are almost perpendicular to the substrate surface [49].

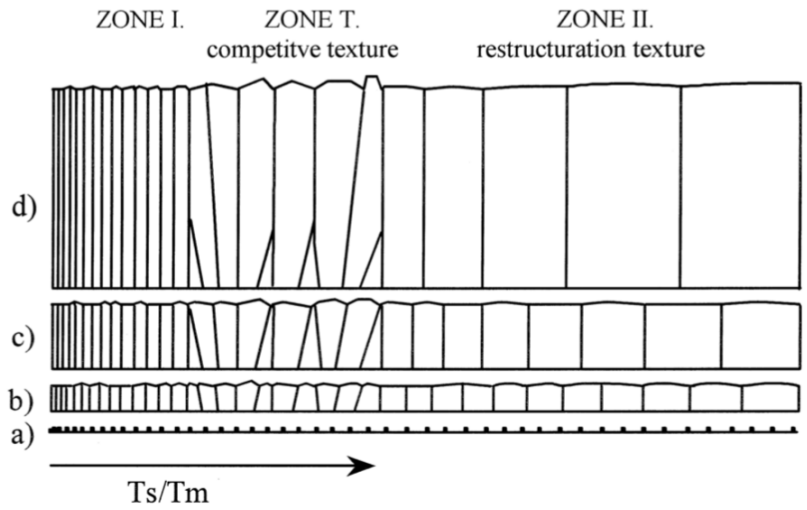

Figure 2.3: Basic SZM applied at different film thicknesses [49].

As the diffusion processes accelerate with increasing T_s/T_m, the diameter of the columns increases as well. It is also obvious in Figure 2.3 that the surface in this zone is smoother than in Zone T, which shows a particularly rough appearance. This restructuring growth texture is a result of the high mobility of the grain boundaries at these temperatures [49]. Neighbouring crystals grow together and only grains with low energy orientations remain.

The shadowing effect and high energy bombardment

The porous structure in Zone I is a result of the shadowing effect at low temperatures, where diffusion processes are limited and do not reconcile the thermodynamic imbalance. The atoms approaching the substrate attach preferably to the peaks rather than to the valleys of a surface [46, 47]. This means, that an already established surface roughness but also a low deposition angle favour the voided Zone I texture and delay the formation of the Zone T to higher temperatures.

An oblique deposition angle can be constructed by tilting the substrate to generate a specific texture. But more often it is a consequence of a high gas pressure in the deposition chamber or hollow cathode sputtering. The first causes more opportunities of scattering from the line-of-sight path of the sputtered atoms [46, 47]. To avoid such oblique flux, and therefore gain a denser structure, it is advisable to reduce the total gas pressure or, in the case of a hollow cathode, to apply shields that restrict the material flux [47].

Another way to densify and potentially eliminate the columnar structure of a deposition is the implementation of high energetic particle bombardment [47, 48, 52]. By re-sputtering the atoms located at the roughness peaks, these are manipulated to fill valleys and to form a smoother surface. This ensures increasing nucleation rates for newly sputtered atoms.

Also the bombardment may cause an impact to drive atoms in the near surface area further into the bulk material and fill voids that are already existing in the microstructure [46, 52].

Bombarding particles, that are used most often, are ions from the plasma or an additional ion source. These ions are then accelerated by applying a bias voltage to the substrate. Other particles include sputtered atoms and neutralised ions that are reflected from the target surface [46]. The latter ones are especially of interest due to a higher energy. This energy is influenced by the target to working gas mass ratio [52]. However, a significant disadvantage to this method is an increased incorporation of working gas atoms, which changes the chemical composition of the film [46, 47, 52].

The influence of impurities

As aforementioned, the microstructure not only depends on temperature, but also on the magnitude of impurities. Introducing a multicomponent structure, the microstructure may vary significantly from the expected texture according to the basic SZM. Due to the incorporation of a different element, the mobility of grain boundaries is usually inhibited causing a decreased grain size. There are only a few exceptions, such as alloying Sn to Al, which show an opposite effect and promote the grain growth [48].

As shown in Figure 2.4, the blocking of grain boundaries results in narrow columns, competitive growth textures or eventually globular crystals for respectively small, medium or high concentrations of impurities [48, 49]. The latter one is also described in some SZMs as Zone III. This structure appears at very high temperatures ($T_s/T_m > 0.5$) and/or high concentrations of impurities. Obviously this structure is a result of a high potential for bulk diffusion. Only at elevated diffusion rates, incorporations are able to segregate to the grain boundaries or the surface of a growing crystal hindering additional growth and leading to a conversion of the columnar structure to equiaxed three dimensional grains with randomly oriented lattice planes [47–49]. A very high concentration of impurities may lead to a nano-crystalline or even amorphous structure [49].

2.3 Thin Film Characterisation

2.3.1 Mechanical Properties

A common method to investigate the mechanical properties of thin films is nanoindentation. With this technique, typically a so-called Berkovich diamond indenter, an indenter in the shape of a three-sided pyramid, is pressed into a surface and the load is recorded as

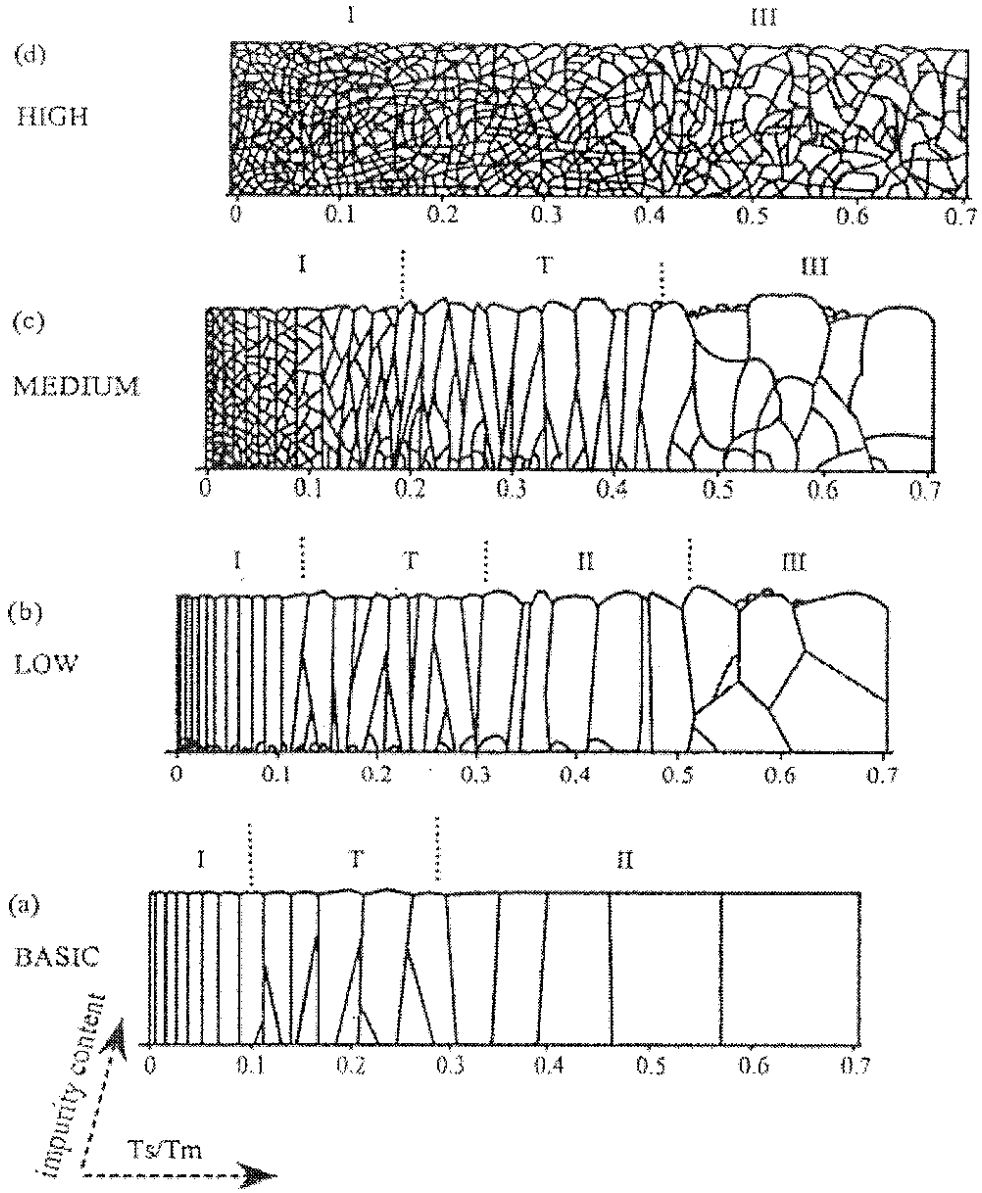

Figure 2.4: Formation of the microstructure in dependence of the homologous temperature and qualitative concentration of impurities [53].

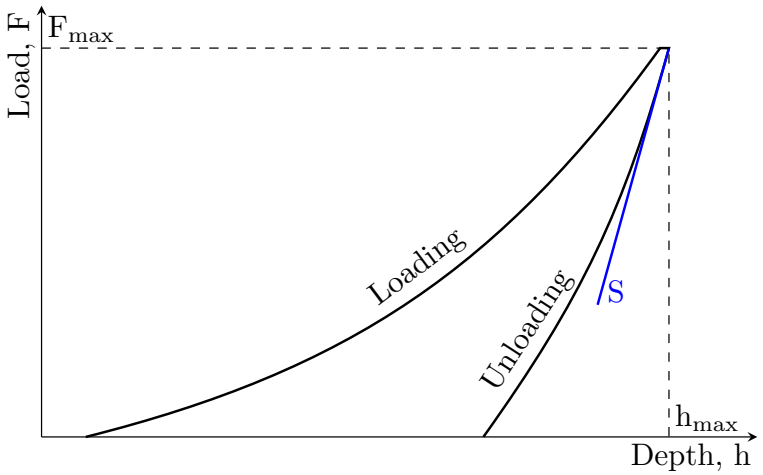

Figure 2.5: Schematic illustration of the loading and unloading curves of nanoindentation analysis (after [54, 55]).

a function of the penetration depth during loading and unloading, as schematically shown in Figure 2.5. From the resulting curves, the stiffness S of the material is determined as the slop of the unloading curve at the maximum load $F_{\max}$ and total depth $h_{\max}$. Subsequently, from the contact depth h_c and thereby the contact area A_c, the hardness H and the reduced modulus E_r can be calculated according to Eq. (1)-(3) [54, 55]. The constants η and β are a geometry factor of 0.75 for the Berkovich tip and a dimensionless parameter close to unity, respectively [55]. If the Poisson's ratio ν of the material and the elastic properties of the tip (E_i, ν_i) are known, the Young's modulus E of the film could be computed as well.

$$h_c = h_{\max} - \eta \frac{F_{\max}}{S} \tag{1}$$

$$H = \frac{F_{\max}}{A_c\left(h_c\right)} \tag{2}$$

$$E_r = \frac{\sqrt{\pi}}{2\beta\sqrt{A_c\left(h_c\right)}} S = \left(\frac{1-\nu^2}{E} + \frac{1-{\nu_i}^2}{E_i}\right)^{-1} \tag{3}$$

The ratio of hardness to Young's modulus H/E is an indicator for the resistance to cracking and plastic deformation and typically correlates well with the wear resistance of a material [56]. The total area underneath the loading and unloading curve represents the work that was performed to deform the material both, elastically and plastically. Hence, the area underneath the unloading curve corresponds to the work performed for elastic deformation and the area between the loading and unloading curve corresponds to the work performed for plastic deformation. By dividing the area underneath the unloading curve by the total area, the elastic deformation that is restored after unloading is determined. This restored deformation is the so-called elastic recovery.

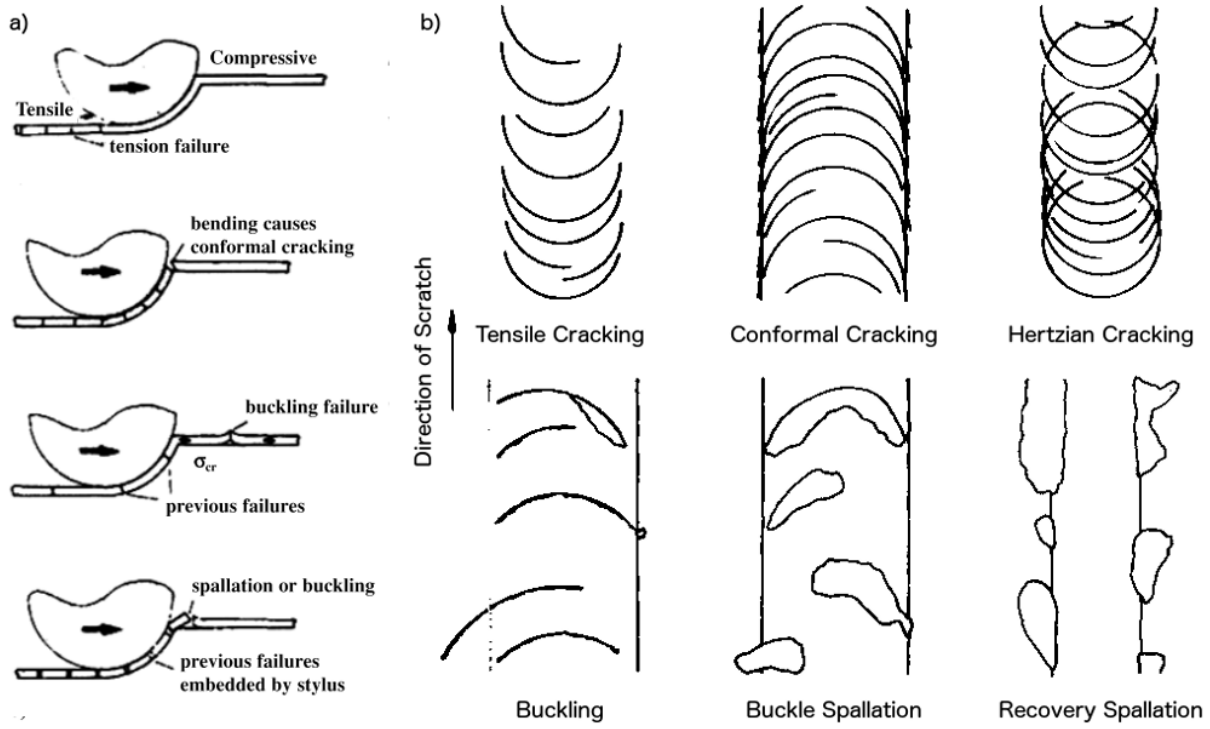

Figure 2.6: Typical failure modes during scratch testing outlined in a) cross sectional and b) top view (after [58, 59]).

Information of the wear and also adhesion behaviour of a film is provided by scratch testing, where a conical diamond tip with a specified tip radius is scratched over a surface [57]. There are different scratching modes at which the load increases, decreases or is kept constant over a certain scratching length. Typical failure modes, as shown in Figure 2.6, can be tensile cracks that occur as a result of tensile stresses behind the tip, conformal cracks that are induced by the bending of the film into the scratch track and Hertzian cracks that originate at a mismatch of elastic behaviour between the coating, the substrate or the tip material in contact. Also spallation of the film and chipping of the substrate can appear during scratching, where the first is either a result of buckling ahead of the scratching tip or because of elastic recovery behind the tip. The latter stems from a hard film deposited on a hard substrate showing good adhesion properties [58, 59]. The behaviour of the film-substrate-system is influenced by the thickness of the film, the scratching speed, the loading rate, but also by the properties of the film and the substrate, such as hardness and Young's modulus. Also internal stresses in the film and the friction between the scratching tip and the film have an effect on the results [58–60]. The critical load at which the first crack appears is called L_{C1} and the load, where the substrate is first exposed due to adhesive failure is called L_{C2} [57].

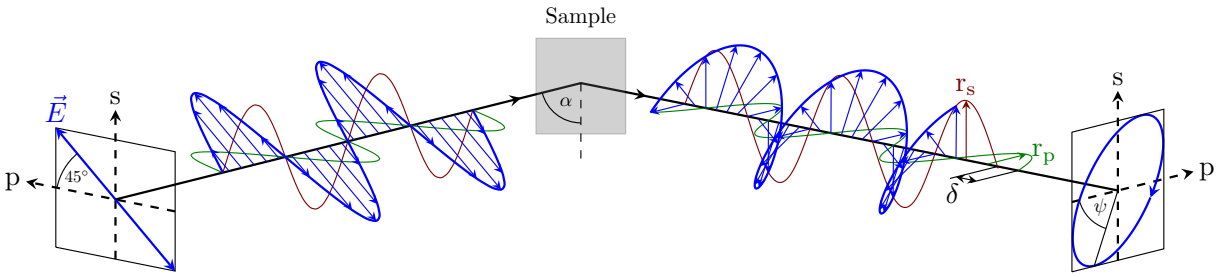

Figure 2.7: Schematically illustrated principle of the light path during a spectroscopic ellipsometry measurement (after [62]).

2.3.2 Optical Properties

When light approaches a surface, it is partly reflected, partly transmitted and partly absorbed by the material. To what extent each interaction occurs, depends on the material and the wavelength of the light. There are different atomistic theories to describe this behaviour, e.g. postulated by Hagen and Rubens, Drude or Lorentz [61]. The amount of reflection R, transmission T or absorption A of light can be measured by its intensity loss. Surface roughness, grain boundaries and impurities in the microstructure may additionally cause scattering S [42]. The sum of the intensities of light after these interactions needs to correspond to the intensity of the incident light

$$I_0 = I_\mathrm{T} + I_\mathrm{R} + I_\mathrm{A} + I_\mathrm{S}. \tag{4}$$

Metals typically exhibit a high reflectance in the visible range that decreases drastically at a so-called plasma frequency [61]. Insulators, such as oxides and fluorides, on the other hand, show often high transmission in the visible and infrared range but are absorbing in the ultraviolet region [42]. This transition occurs at the so-called absorption band edge.

Light, as an electromagnetic wave, changes its direction, velocity and wavelength upon entering a material as a consequence of electric charges [42, 61]. Yet, the energy and thereby the frequency of the light wave is constant. This phenomenon is called refraction and is quantified by the complex refractive index

$$N = n - ik, \tag{5}$$

where n is the real refractive index and k is the extinction coefficient. The refractive index expresses how the wave velocity changes at the interface of two different materials, while the extinction coefficient indicates the absorption behaviour in the second material. For insulators the latter one is usually close to zero, yet, for metals and metal-like materials the refractive index and extinction coefficient are of similar magnitude [42].

In order to determine the refractive properties of a thin film, a spectroscopic ellipsometer can be used that measures the changed polarisation state of a reflected light wave compared to the incident light [61–65]. Therefore, plane-polarised light with an angle of 45° to the plane of incidence and a specific electric field strength E is reflected on a surface under a certain incident angle α, as shown in Figure 2.7. This reflected light is consequently elliptically polarised, which can also be described as two plane-polarised light waves along two orthogonal axes with a phase difference δ. The amplitude reflection coefficients, that are parallel r_p and perpendicular r_s to the plane of incidence, generate a vibrational vector with an angle ψ against the plane of incidence. The ellipsometry parameters ψ and δ can therefore be determined by measuring the ratio of the amplitude reflection coefficients

$$\rho = \frac{r_\mathrm{p}}{r_\mathrm{s}} = \tan(\psi) e^{i\delta} \tag{6}$$

and displayed as a function of wavelength and incident angle. Further on these can be converted into the complex dielectric constant

$$\epsilon = \epsilon_1 - i\epsilon_2, \tag{7}$$

$$\epsilon_1 = \sin^2\alpha \left[1 + \frac{\tan^2\alpha \left(\cos^2 2\psi - \sin^2 2\psi \sin^2\delta\right)}{\left(1 - \sin 2\psi \cos\delta\right)^2}\right], \tag{8}$$

$$\epsilon_2 = -\frac{\sin 4\psi \sin\delta \tan^2\alpha \sin^2\alpha}{\left(1 - \sin 2\psi \cos\delta\right)^2}, \tag{9}$$

where ϵ_1 is related to the polarisation and ϵ_2 corresponds to the absorption [61]. Subsequently, the complex dielectric constant can be converted into the complex refractive index

$$\epsilon = N^2 = n^2 - k^2 - i2nk. \tag{10}$$

To evaluate the obtained results, a model describing the behaviour of the reflected light beam needs to be built. Typical functions used for that purpose are the Lorentz, the Tauc-Lorentz, the Gaussian or the Drude function. Additional information about the film system, that can be determined with this technique, are the surface roughness and the thickness of optically transparent layers. It is also sensitive to inhomogeneities in the microstructure, such as crystallinity, texture and gradients. To get more reliable results, those inhomogeneities should be identified beforehand and can be included into the model [64].

2.3.3 Electrical Properties

The way a material reacts to an externally applied electric field is expressed by its electrical conductivity, the reciprocal to the electrical resistivity, which in turn is defined as the

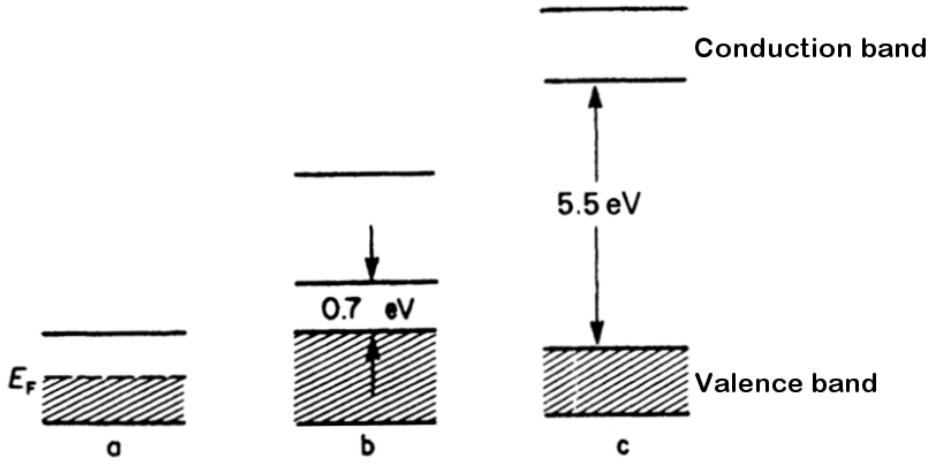

Figure 2.8: Band model illustrated schematically for a) metals, b) semiconductors, e.g. germanium, and c) insulators, e.g. diamond (after [61]).

specific electrical resistance of a material. In the classical electron theory, postulated by Drude, the conductivity of a material depends largely on the number of free electrons and their mobility in an electric field. Considering the quantum mechanical approach shows that not all free electrons contribute to the conductivity. The more electrons are located near the Fermi energy E_F, which marks the highest energy level occupied by electrons at 0 K, the higher is the conductivity of a material [42, 61].

In quantum physics each material can be characterised according to its electric band structure. Electric bands are the energy regions electrons are permitted to occupy. The highest energy region filled with electrons is called the valence band and the next higher unfilled band is the conduction band. In metals the valence band overlaps the conduction band and is only partially filled. It is therefore fairly easy for electrons to move freely and enhance conductivity. Insulators and semiconductors show completely filled valence bands and the conduction band is separated by a material specific gap energy E_g. For semiconductors this gap is relatively narrow and electrons are able to overcome the forbidden zone by absorbing additional energy from, e.g., phonons or photons [61]. A simplified illustration of this concept is depicted in Figure 2.8. For metals (Figure 2.8a) the position of the E_F is indicated, for all other materials the position of the E_F is in between the valence and the conduction band. An E_g of 0.7 eV and 5.5 eV is characteristic for germanium, a semiconductor, and diamond, an insulator, respectively.

The four point probe analysis is an approved method for determining the resistivity of materials, especially semiconductors. With this technique four electrodes are arranged in a line with equal distance functioning as two separate circuits. The two electrodes on the outside inject a current into a flat surface, while the two electrodes at the inside measure

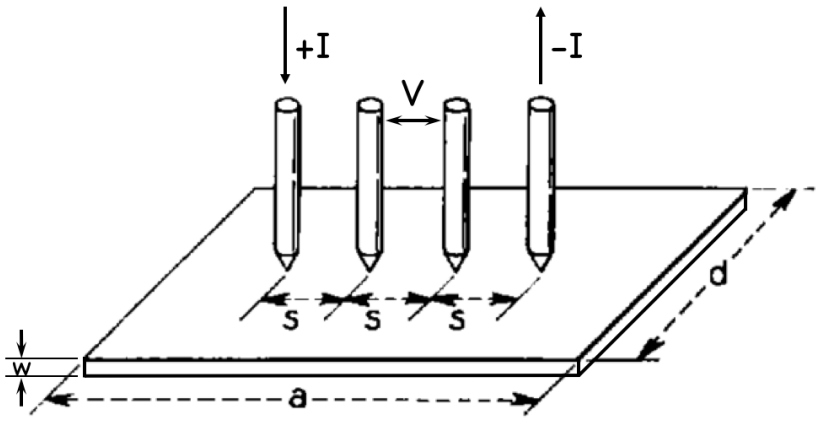

Figure 2.9: Principle of the four point probe measurement, (after [68]).

the resulting potential, as shown in Figure 2.9 [66, 67]. The accuracy of the measurement depends on the geometry of the thin film, the surface condition, the position of the probe and the conductivity of the substrate [66].

By applying a specific correction factor to the measured resistance, the aforementioned source of error for different geometries is minimised [68]. Subsequently, the corrected resistance is multiplied by the film thickness to obtain the resistivity ρ, which is also expressed by

$$\rho = \frac{V}{I} C \left(\frac{a}{d}; \frac{d}{s} \right) w, \tag{11}$$

where V is the voltage and I the current, which, as a ratio, represent the measured resistance according to Ohm's law. C is the correction factor that depends on the relations between a, d and s, i.e. the length and the width of the sample and the distance between the electrodes of a four point probe, respectively, and w is the film thickness.

3 Experimental Details

The Mo-O-N thin films were synthesised by DC reactive magnetron sputter deposition using an industrial scale in-line deposition system (FHR.Line.600-V) with a cylindrical rotatable Mo target (⌀152 mm × 600 mm). The distance from the target to the substrate holder was approximately 75 mm. All films were prepared on soda lime glass (25 mm × 25 mm × 1 mm) and (100)-oriented silicon (21 mm × 7 mm × 0.325 mm).

After placing the substrates on the carrier in the load-lock chamber, the latter was evacuated to a pressure below 1×10^{-5} mbar and the valve of the deposition chamber was opened. The base pressure prior to the deposition process was about 1×10^{-6} mbar. In order to remove surface contamination from the substrates and to enhance the adhesion of the deposited Mo-O-N films, the substrates were plasma etched in a RF discharge at a constant Ar gas pressure of 3.4×10^{-3} mbar and a constant power of 0.8 kW. During deposition the discharge power was set to 2 kW and no external heating was applied to the grounded substrate carrier. For the deposition of the Mo-O-N films, a total gas flow of 100 sccm was applied, which corresponds to a total pressure of 1.5×10^{-3} mbar. As illustrated in Table 3.1, this means for the metallic Mo films an Ar flow of 100 sccm was used, while for the Mo-O-N films the Ar flow was 40 sccm and the total reactive gas flow was 60 sccm. In the further course of this work, the samples will be identified by their reactive gas flow ratio, which is also displayed in Table 3.1.

As shown in Figure 3.1, an initial Ar flow of 150 sccm was needed to ignite the plasma. After ignition, the Ar flow was reduced to the steady-state value (see Table 3.1), which was reached after 10 s. This change in Ar flow caused an increase in the discharge voltage, while the discharge current decreased as a consequence of the applied constant power. Subsequently, when the Ar flow was kept constant, the discharge voltage and current stabilised. Figure 3.2 shows how these stabilised values changed for different gas flow

Table 3.1: Variation of Ar, O_2 and N_2 gas flow rates during deposition of Mo-O-N films.

Ar flow [sccm]	100	40	40	40	40	40	40	40
O_2 flow [sccm]	0	60	50	45	40	30	20	0
N_2 flow [sccm]	0	0	10	15	20	30	40	60
Reactive gas flow ratio $\frac{N_2}{O_2+N_2}$ [%]	-	0	17	25	33	50	67	100

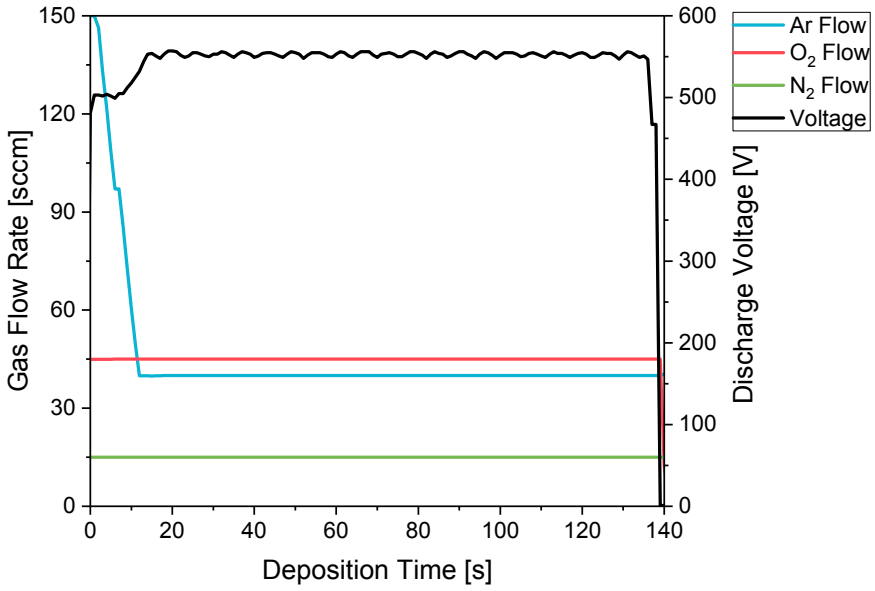

Figure 3.1: Ar, O_2 and N_2 gas flow rates and discharge voltage as a function of time during the deposition of the 200 nm thick Mo-O-N films grown at a gas flow $N_2/(O_2+N_2)$ ratio of 25 % film to illustrate the plasma ignition procedure.

$N_2/(O_2+N_2)$ ratios and varying film thicknesses. A change in the discharge voltage is linked to the electron emission of the target, which is affected by the poisoning mode of the target [18]. The discharge voltage increases with gas flow $N_2/(O_2+N_2)$ ratios increasing up to 50 % from about 550 V to almost 600 V. With further increase of the gas flow $N_2/(O_2+N_2)$ ratio the discharge voltage decreases below 500 V. The lowest value is observable for the metallic Mo film that shows a discharge voltage of about 350 V. The discharge current shows the opposite trend than the voltage, since the deposition process was operated at a constant power. The variation in discharge voltage and current with different thicknesses is probably due to the fact that the different series were not deposited all at once, but at different time frames. Hence, the general state of the deposition system could have been slightly different.

Three series of Mo-O-N films, including a reference Mo film, with nominal film thickness of 100 nm, 200 nm and 1000 nm were synthesised. Additionally, thin films with thicknesses of 40 nm and 70 nm were prepared for selected film compositions. The deposition time was adjusted with varying reactive gas flow ratio. For this purpose, preliminary test depositions with constant deposition time were conducted. The film thickness of the films from the test depositions was determined using an optical 3D white light profiling system (Wyko NT 1000) and the growth rate, subsequently, calculated by dividing the thickness by the deposition time.

To determine the thickness of the synthesised Mo-O-N series, spectroscopic ellipsometry

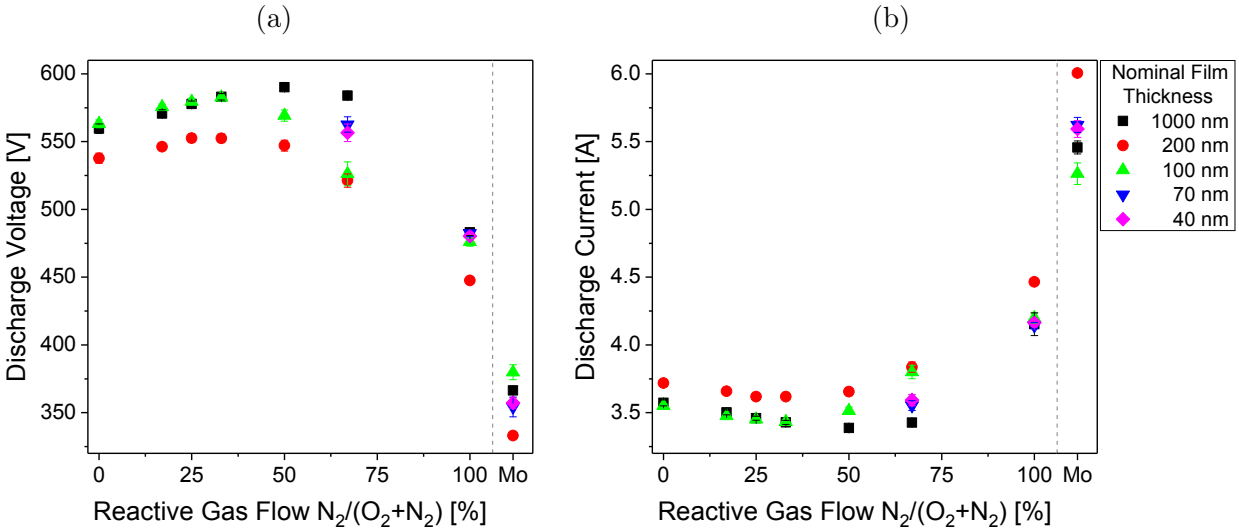

Figure 3.2: Average steady-state values of (a) discharge voltage and (b) discharge current during the sputter deposition of Mo-O-N films grown at different reactive gas flow ratios and of Mo films, separated by a dashed line, for different nominal thicknesses.

(SE) (J.A. Woollam Co. RC2 Ellipsometer) was used. Measurements were conducted at four different incident angles of the light beam, namely at 45°, 55°, 65° and 75°. A generalised oscillator layer with Tauc-Lorentz as a base function was used to build a model that fits the material's behaviour when exposed to polarised light. When needed, additional functions such as a Gaussian or, for conductive materials, the Drude function were built in. To get more reliable models, the transmittance measurements were included in the model as well. If necessary, the models for the films with a film thickness below 100 nm were modified with a gradient due to the inhomogeneity caused by the drop in Ar flow during the plasma ignition. The thickness of the films that were too opaque and hence prevented the determination of the film thickness by SE, such as the Mo film and the Mo-O-N film grown at a gas flow $N_2/(O_2{+}N_2)$ ratio of 100 % with a thickness of more than 200 nm, was measured with a mechanical profilometer (Bruker DektakXT Stylus Profiler).

The composition of selected samples with a nominal thickness of 200 nm was measured with elastic recoil detection analysis (ERDA) (Tandem 6 MV accelerator) using Co ions with an energy of 50 MeV. The analysed area was about 2 mm × 2 mm. X-ray photoelectron spectroscopy (XPS) (VG ESCALAB 3 MKII) was additionally used to analyse the binding energies and the composition at the surface of the films. By comparing the composition obtained by ERDA and by XPS, information on the oxidation state at the surface of the compounds was obtained. The XPS analysis was carried out with a Mg-K_α (1253.7 eV) source operated at 300 W (15 kV, 20 mA) and a pressure in the analysis

chamber of about 4×10^{-9} mbar. The samples were measured as received at an area of 2 mm × 3 mm. The pass energy for survey scans was 100 eV with a step size of 1 eV, while the pass energy for high resolution scans was 20 eV with a step size of 0.05 eV. The background was subtracted according to the Shirley method and the charge correction was calibrated with respect to the C1s peak at 284.8 eV. Electron dispersive X-ray spectroscopy (EDX) (Oxford Instruments INCA) implemented in a scanning electron microscopy (SEM) (Zeiss EVO50) was used to verify the chemical composition of the Mo-O-N film grown without addition of O. The microstructure was analysed using SEM imaging (Hitachi S-4700) and X-ray diffraction (XRD) (Bruker D8 Discover). For the latter, films with a nominal thickness of 1000 nm deposited on glass were examined. Selected samples with thinner film thickness or deposited on Si were measured as well to ensure the consistency of the diffractograms. The measuring mode was grazing incident with a Cu-K_α beam (λ=0.154 06 nm) at an incident angle of 1°. The measurements were carried out at 2θ angles between 20 and 90° with increments of 0.02° and a holding time of 1 s/step.

The mechanical properties, such as hardness H and reduced modulus E_r of the samples with a nominal thickness of 1000 nm and deposited on Si, were investigated with nanoindentation measurements (Hysitron Ubi-3). Also the elastic recovery was determined by dividing the area underneath the indentation loading curve by the area underneath the unloading curve and corresponds to the elastic deformation that was restored after unloading. The ratio between H and E_r that describes the 'elastic strain to failure' was determined as well [56]. Micro-scratch tests (CSM Instruments micro combi tester) were performed on the 1000 nm thick Mo-O-N films deposited on glass. The diamond tip radius was 200 μm and the load continuously increased from 0.02 to 30 N over a scratch length of 7.5 mm.

The SE measurements were also used to obtain the refractive index, the extinction coefficient and the band gap of all samples coated on glass. Information about the transmittance and reflectance were gathered for the same samples with spectrophotometry (Agilent Technologies UMA Cary 7000) at a wavelength range between 250 and 850 nm. The absorption was then calculated by subtracting the normalised intensity of transmittance and reflectance from unity.

To investigate the electrical resistivity of the films, a four point probe connected to a voltmeter (Hewlett Packard 34401A Multimeter) and a current source (Keithey 220 Programmable Current Source) was used. The measurements were conducted on the films deposited on the glass substrate and the correction factor for the sample's geometry was determined according to Smits [68].

4 Results and Discussion

4.1 Thickness and Chemical Composition

The individual thickness of each sample as well as the average thickness of the different series are displayed in Figure 4.1. The growth rates of each series as a function of the flow rates of the reactive gases are shown in Figure 4.2. The Mo-O-N films show generally decreased growth rates, hence slower film growth, compared to the pure Mo film, which is a result of target poisoning effects. It is also obvious that the growth rate increases with increasing gas flow $N_2/(O_2+N_2)$ ratio up to 50 % by a factor of about 1.5, whereas with further increase in the gas flow $N_2/(O_2+N_2)$ ratio the growth rate decreases again. A similar behaviour of the growth rate with varying reactive gas flow rate was also observed in literature for both MoO_x and MoN_x films [18, 69]. For the MoO_x, the initial increase in growth rate observed in Ref. [18] was explained by the higher availability of O with increasing O_2 partial pressure up to 50 %. In that region the sputter rate of the Mo target was mostly unaffected, hence, with increasing O_2 flow rates, there were more species present in the deposition chamber that form the MoO_x film. In the present case, however, the reactive gas flow is constant and only changing from an oxygenous to a nitrogenous atmosphere. The availability of reactive species should therefore be similar for all synthesised Mo-O-N films. The O_2 gas, however, is more likely to react with Mo than the N_2 gas, as more energy is required to form a N^{3-} ion than an O^{2-} ion. The reason is the higher binding energy of N_2 compared to O_2 and the higher electron affinity of N than that of O [11]. With an increase in N_2 flow rate the O_2 flow rate is decreasing, which could result in a reduction of the target poisoning effect. Therefore, the growth rate is increasing at low gas flow $N_2/(O_2+N_2)$ ratios. The decrease in growth rate at gas flow $N_2/(O_2+N_2)$ ratios higher than 50 % is most likely a consequence of the target poisoning effect due to the N.

The described trend in growth rate with changing reactive gas flow ratio can be observed for all Mo-O-N series. However, as depicted in Figure 4.2, the 1000 nm thick films show decreased values compared to the series with nominal thicknesses of 200 nm and below. This indicates that the growth rate is not constant, but decreases with progressing deposition time. A possible explanation can be the elevated Ar flow rate during the plasma ignition sequence, as demonstrated in Figure 3.1, where a higher growth rate was present due to an increased Ar/O_2 ratio and no target poisoning effects have occurred yet. The duration of the sequence was 10 s, which corresponds to only about 1 % of the deposition time of the 1000 nm films, but about 8 % and 15 % of that of the 200 and 100 nm films,

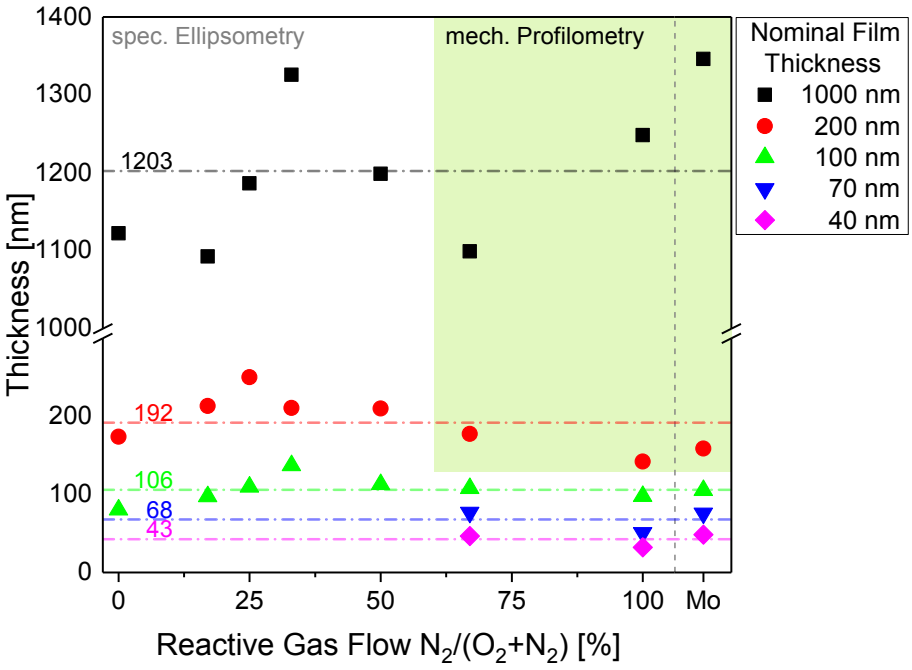

Figure 4.1: Film thickness for the Mo-O-N films as a function of reactive gas flow ratio and for Mo films (right), separated by a dashed line. The deposition time was adjusted to achieve the nominal film thickness. The horizontal dashed lines indicate the average value of each series.

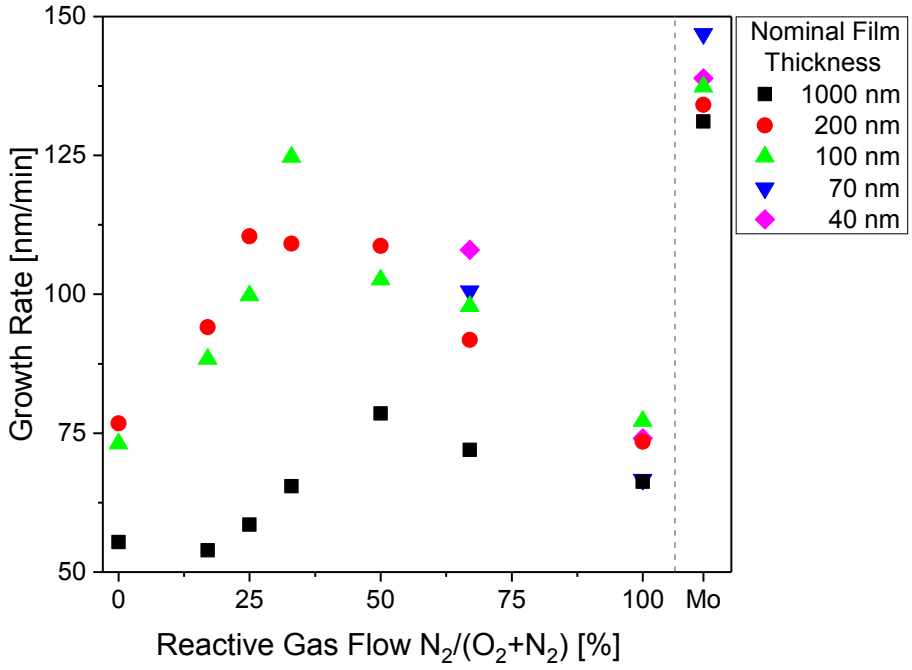

Figure 4.2: Growth rate of the synthesised Mo-O-N films as a function of the reactive gas flow ratio and of the Mo films (right), separated by a dashed line, for different series with varying film thickness.

respectively. Hence, its influence should be more pronounced the thinner the film is. But also other factors such as a densification of the films during the deposition procedure or the general state of the industrial-size deposition system during deposition of each series need to be considered. For Mo-O-N film grown at a gas flow $N_2/(O_2+N_2)$ ratio of 100 % and the pure Mo film, there is only a slight change in the growth rate with variation in thickness noticeable. This could indicate that the influence of a variation in Ar/N_2 or the target poisoning effect are not as significant as for MoO_x.

The chemical composition of selected films of the 200 nm series is displayed in Figure 4.3, which summarises the results of both, the ERDA and the XPS measurements. With ERDA an average value of the atomic content over the whole film thickness is determined, while with XPS only the composition at the surface of the film is measured. When comparing the ERDA results to the outcome of XPS, it is noticeable that there is hardly any difference for the samples grown at low gas flow $N_2/(O_2+N_2)$ ratio, but for films with a high gas flow $N_2/(O_2+N_2)$ ratio the O content determined by XPS is significantly higher compared to ERDA. For the Mo-O-N film grown at a gas flow $N_2/(O_2+N_2)$ ratio of 67 %, N is almost completely substituted by O and even for the Mo-O-N film grown at a gas flow $N_2/(O_2+N_2)$ ratio of 100 % there is as much O as N present at the film surface. This comparison reveals that all deposited Mo-O-N films naturally oxidise on their surface and techniques that penetrate deeper into the films like ERDA are necessary in order to determine their actual chemical composition.

Considering only the ERDA results, a significant increase of the N content is obvious for a reactive gas flow ratio of 50 % and higher. As the N content increases, the O level in the film decreases. Also the Mo content increases with the gas flow $N_2/(O_2+N_2)$ ratio, rising from 20 to 40 at.%. The delayed incorporation of N towards higher gas flow $N_2/(O_2+N_2)$ ratios is the result of a higher reactivity of O compared to that of N [11]. At lower gas flow $N_2/(O_2+N_2)$ ratios, where no measurable N is incorporated, the high Ar/O_2 ratio leads, as previous studies have shown, to the formation of lower oxidised MoO_x compounds, hence the formation of O vacancies [17, 18].

ERDA measurements of the Mo-O-N film grown at a gas flow $N_2/(O_2+N_2)$ ratio of 100 % yield a N content of around 60 at.%. However, according to literature this value usually does not exceed 50 at.%. Only a few publications are known that show a higher value, yet the reason remains unexplained [70]. However, additional measurements with EDX confirmed the high N content in the Mo-O-N film grown at a gas flow $N_2/(O_2+N_2)$ ratio of 100 % with about 55 at.%.

Figure 4.4 shows the core level spectra of the Mo-O-N films grown at gas flow $N_2/(O_2+N_2)$ ratios of 0 %, 67 % and 100 % as determined by XPS. The core levels of the Mo-O-N film

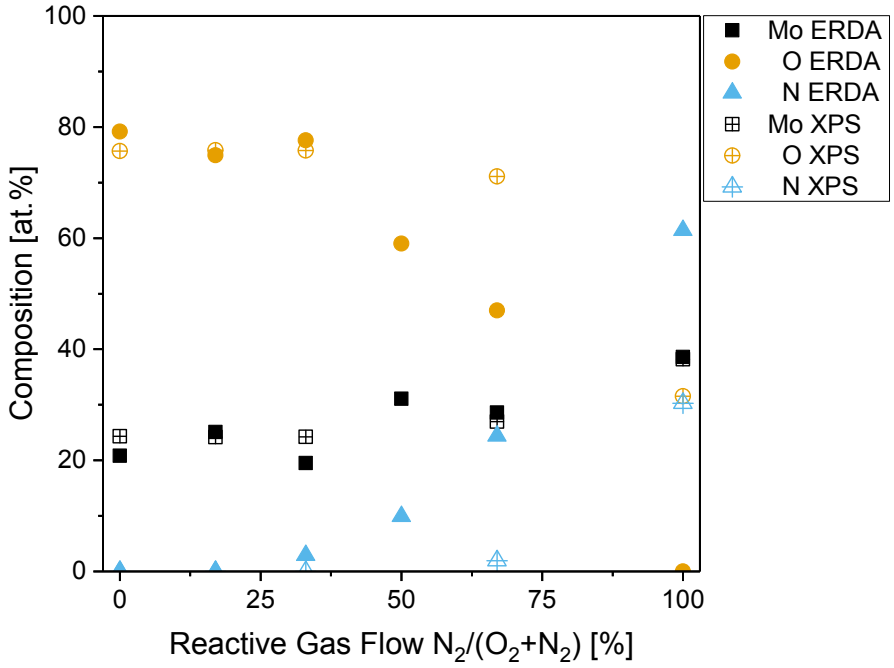

Figure 4.3: Chemical composition of the Mo-O-N films as a function of the gas flow $N_2/(O_2+N_2)$ ratio determined by ERDA (filled icons) and XPS (crossed icons). The film thickness is approximately 200 nm.

grown at a gas flow $N_2/(O_2+N_2)$ ratio of 0 % are representative for the Mo-O-N films grown at gas flow $N_2/(O_2+N_2)$ ratios of 50 % and lower. Although the measurements were conducted on the naturally oxidised surfaces, there is an obvious change in the oxidation state of Mo with increasing gas flow $N_2/(O_2+N_2)$ ratio. The highest oxidation state of Mo observed in all synthesised films is Mo^{6+}, which indicates the formation of the MoO_3 phase at low gas flow $N_2/(O_2+N_2)$ ratios. In addition, the oxidation states Mo^{5+} and Mo^{4+} point towards the presence of lower oxidised MoO_x phases at higher gas flow $N_2/(O_2+N_2)$ ratios. Mo-N bonds were only detected for the Mo-O-N films grown at gas flow $N_2/(O_2+N_2)$ ratios of 67 % and 100 %. It is obvious, that the number of Mo-N or N-Mo bonds, in the N1s core level spectra, increase with gas flow $N_2/(O_2+N_2)$ ratios higher than 67 %, while the number of Mo^{6+} or O-Mo bonds, in the O1s core level spectra, are decreasing. In the N1s core level spectra additional peaks, that are identified at 401.8 eV as protonated or absorbed ON, are visible. This is a result of the exposure to air after the deposition, since this peak also appears for the Mo-O-N film grown at a gas flow $N_2/(O_2+N_2)$ ratio of 0 %, where no N was present during the deposition. The same is true for the identified O=C and O-C peaks in the O1s core level spectra.

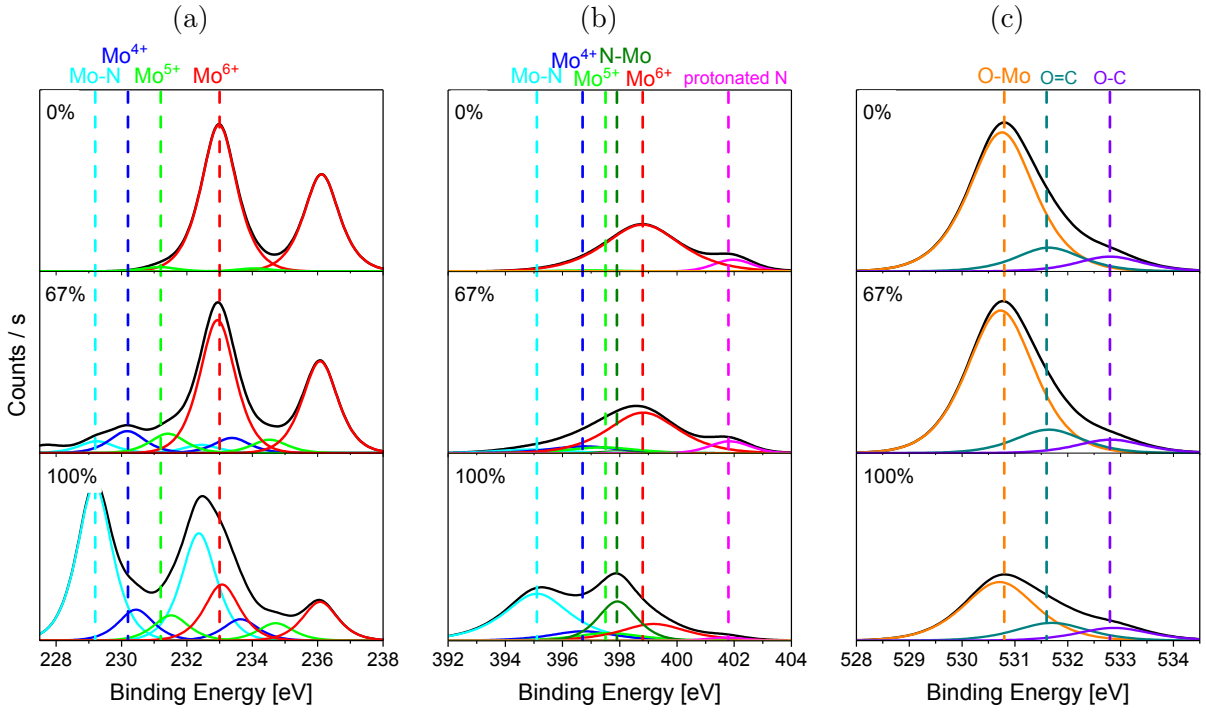

Figure 4.4: a) Mo3d, b) N1s and c) O1s XPS core level spectra of the Mo-O-N films with 0 %, 67 % and 100 % gas flow $N_2/(O_2+N_2)$ ratio. The N1s peak partly overlaps with the Mo3p peak. The film thickness was 200 nm.

4.2 Microstructure

The results of XRD measurements are displayed in Figure 4.5. For the Mo-O-N films rather broad peaks are visible, which indicate very small crystals or even an amorphous structure, which is common for oxides [42]. Although the Mo-O-N films that are rich in O seem to follow the pattern of the MoO_3 phase (ICDD card 00-005-0508), an unambiguous identification of the phases present is not possible with XRD. In literature a similar pattern was found for as-deposited MoO_3 thin films and only after annealing defined peaks were visible [71]. At a reactive gas flow ratio of 50 % and 67 %, where the N content within the films starts to increase, a transition in the diffractograms is visible as the already broad peak is shifted towards the first peak position of the MoN_x phase. Only the Mo-O-N film grown at a gas flow $N_2/(O_2+N_2)$ ratio of 100 %, i.e. without O addition, and the Mo film show a clearly crystalline structure, where the recognised phases are face centred cubic Mo_2N with a lattice parameter of 0.418 nm (ICDD card 00-025-1366) and body centred cubic Mo with a lattice parameter of 0.315 nm (ICDD card 00-042-1120), respectively. The shifted peaks of the Mo-O-N film grown at a gas flow $N_2/(O_2+N_2)$ ratio of 100 % compared to the unconstrained Mo_2N phase corresponds to a higher lattice parameter of 0.425 nm. In literature this phase is characterised as a metastable MoN phase, where more

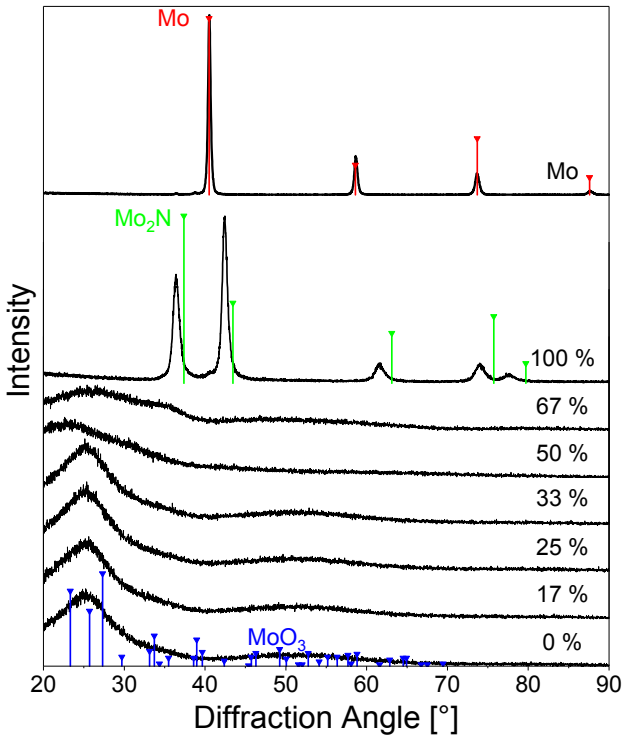

Figure 4.5: X-ray diffractograms of Mo-O-N films with varying reactive gas flow $N_2/(O_2+N_2)$ ratio and the Mo film (top) deposited on glass with a film thickness of 1000 nm.

than 50 % of the octahedral sites of Mo are occupied by N, causing the expansion of the lattice [72, 73]. The high N content of the Mo-O-N film grown at a gas flow $N_2/(O_2+N_2)$ ratio of 100 % of about 55-60 at.% obtained by EDX and XPS measurements, respectively, also agrees more to this metastable MoN phase than to the Mo_2N phase with only 33 at.% of N.

However, this expansion of the lattice, and therefore the increasing incorporation of N, also leads to compressive stresses when constrained by a substrate, which is also confirmed by literature [74]. As this has a higher influence on a thicker film, it was necessary to deposit a interlayer of Mo before depositing the 1000 nm thick Mo-O-N film grown at a gas flow $N_2/(O_2+N_2)$ ratio of 100 % to reduce the lattice mismatch, and therefore the compressive stresses. Otherwise, the Mo-O-N film grown at a gas flow $N_2/(O_2+N_2)$ ratio of 100 % with a film thickness of 1000 nm gradually detaches from the glass substrate.

The X-ray amorphous films are also characterised by a featureless appearance in the SEM fracture cross-section images and seem to have a rather smooth surface, which is depicted in Figure 4.6. Only the Mo-O-N film grown at a gas flow $N_2/(O_2+N_2)$ ratio of 100 % (see Figure 4.6 d) appears to have a columnar growth structure. The Mo interlayer to improve the adhesion on the glass substrate is also visible.

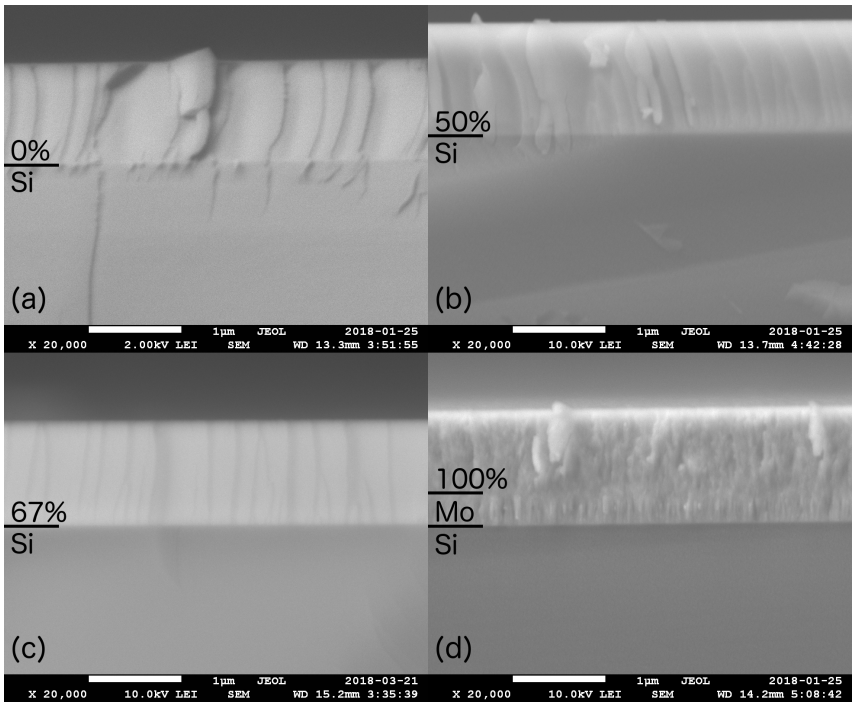

Figure 4.6: SEM fracture cross-section images of the Mo-O-N films grown at gas flow $N_2/(O_2+N_2)$ ratios of a) 0 %, b) 50 %, c) 67 % and d) 100 % with a Mo interlayer. The substrate is Si and the film thickness is 1000 nm.

4.3 Mechanical Properties

The mechanical properties investigated by nanoindentation as a function of the gas flow $N_2/(O_2+N_2)$ ratio are displayed in Figure 4.7. At low gas flow $N_2/(O_2+N_2)$ ratios, hardness and reduced modulus of the Mo-O-N films are lower than those of the Mo film. While the hardness is constant at about 3.2 GPa, the reduced modulus slightly decreases from 67 to 60 GPa with gas flow $N_2/(O_2+N_2)$ ratios increasing up to 50 %. This decrease could be explained by the existence of O vacancies, which, according to previous investigations, leads to a decrease in elastic properties [75]. An increase in both, hardness and reduced modulus can be observed when the gas flow $N_2/(O_2+N_2)$ ratio exceeds 50 %. At this point the first significant amount of N was identified by ERDA measurements, which indicates a substantial influence of N incorporation on the mechanical properties. The highest values for hardness and reduced modulus were recorded for the Mo-O-N film grown at a gas flow $N_2/(O_2+N_2)$ ratio of 100 %, hence the film with the highest N content and the only Mo-O-N film showing a crystalline structure. These values agree to those of MoN_x phases reported in literature [34, 74].

Also the H/E_r ratio and the elastic recovery follow a similar trend. Due to the slight decrease in reduced modulus at gas flow $N_2/(O_2+N_2)$ ratios up to 50 %, the H/E_r ratios

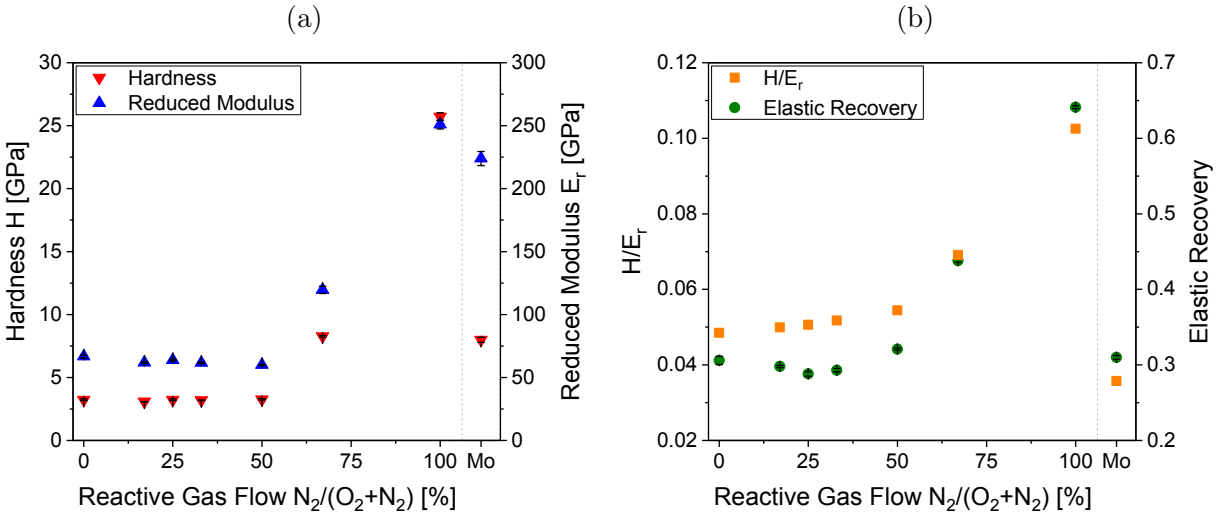

Figure 4.7: a) Hardness H and reduced modulus E_r and b) H/E_r ratio and elastic recovery as a function of the gas flow $N_2/(O_2+N_2)$ ratio. The Mo film (right), as a reference, is separated by a dashed line.

increase in this region. An increased H/E_r ratio correlates to a higher resistance to cracking and decreased plastic penetration [34]. The elastic recovery shows a minimum for the Mo-O-N film grown at a gas flow $N_2/(O_2+N_2)$ ratio of 25 % and is in this region comparable to the elastic recovery of the pure Mo film of about 0.31. This means that about one third of the deformation caused by nanoindentation is elastic, while two thirds of the deformation are irreversible. For gas flow $N_2/(O_2+N_2)$ ratios above 50 %, hence with increasing incorporation of N in the films and increasing crystallinity, both, the H/E_r ratio and elastic recovery increase by a factor of about 2. N incorporation results in harder films with reduced plastic deformation and probably increased wear behaviour, as this is linked to a high H/E_r ratio [56]. The improvement of the mechanical properties due to an increase in N content is in agreement with literature [34, 74].

Figures 4.8 a)-e) display optical images of the scratches obtained at loads higher than 20 N on the Mo-O-N films grown at gas flow $N_2/(O_2+N_2)$ ratios of 0 %, 50 %, 67 % and 100 % as well as the uncoated glass substrate for comparison. The micrograph of the Mo-O-N film grown at a gas flow $N_2/(O_2+N_2)$ ratio of 50 % is representative for those films grown at gas flow $N_2/(O_2+N_2)$ ratios between 0 % and 50 %. Figures 4.8 f)-h) depict higher magnification images, where the failure modes, which are responsible for failure during the scratch tests, can be identified according to literature references [57–59]. The corresponding critical loads for these failure modes are shown in Figure 4.9. For the current testing conditions, the dominant failure type of the uncoated substrate was the formation of Hertzian cracks [57, 58]. These also appeared in the Mo-O-N films, except

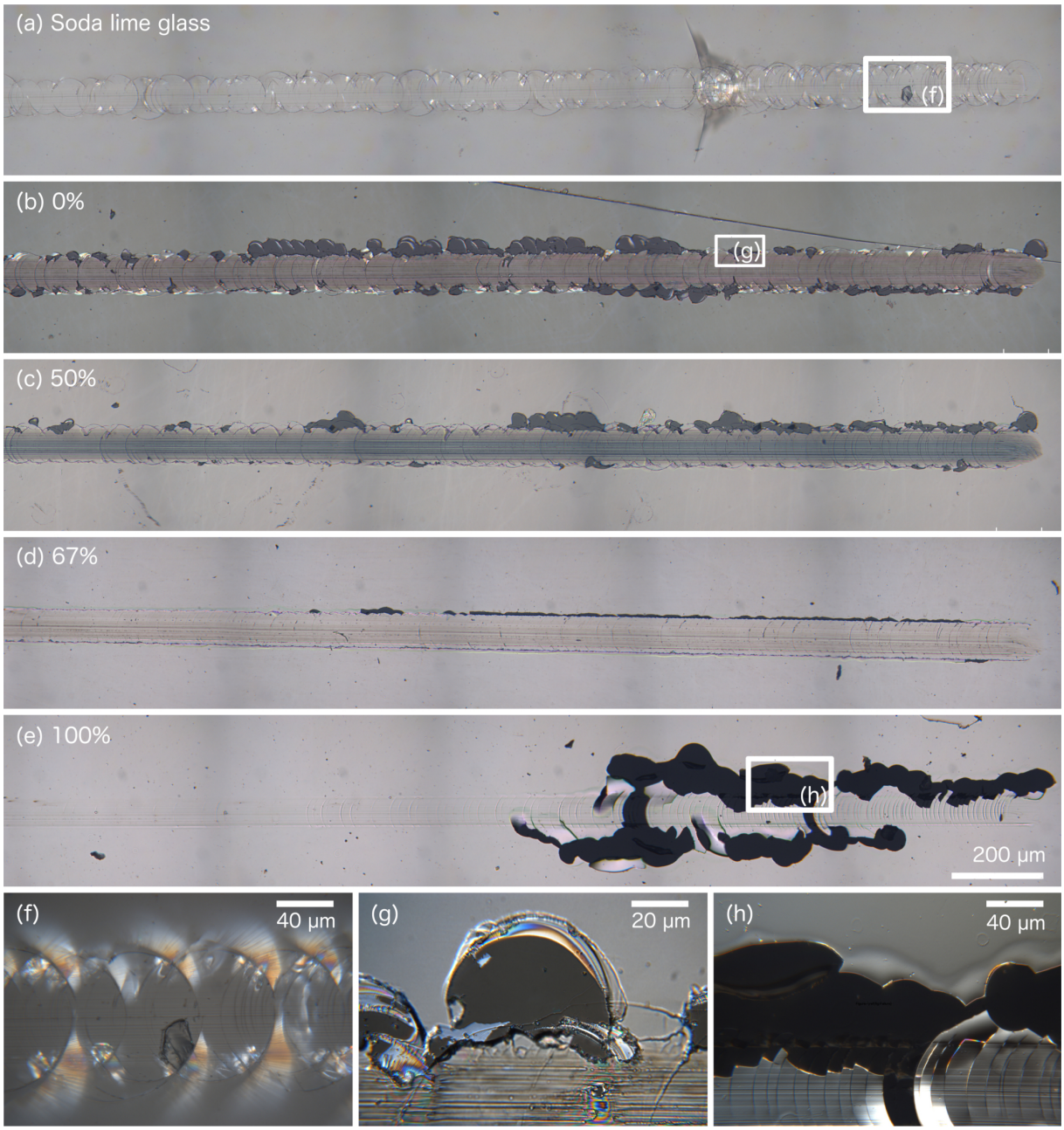

Figure 4.8: Optical micrographs of the scratches on a) the uncoated soda lime glass substrate and the Mo-O-N films grown at gas flow $N_2/(O_2+N_2)$ ratios of b) 0 %, c) 50 %, d) 67 % and e) 100 % and magnifications of the scratches on f) uncoated soda lime glass and Mo-O-N films grown at gas flow $N_2/(O_2+N_2)$ ratios of g) 0 % and h) 100 % to illustrate different failure modes. The nominal film thickness was 1000 nm and the segments in a)-e) show the load regions between approximately 20-30 N.

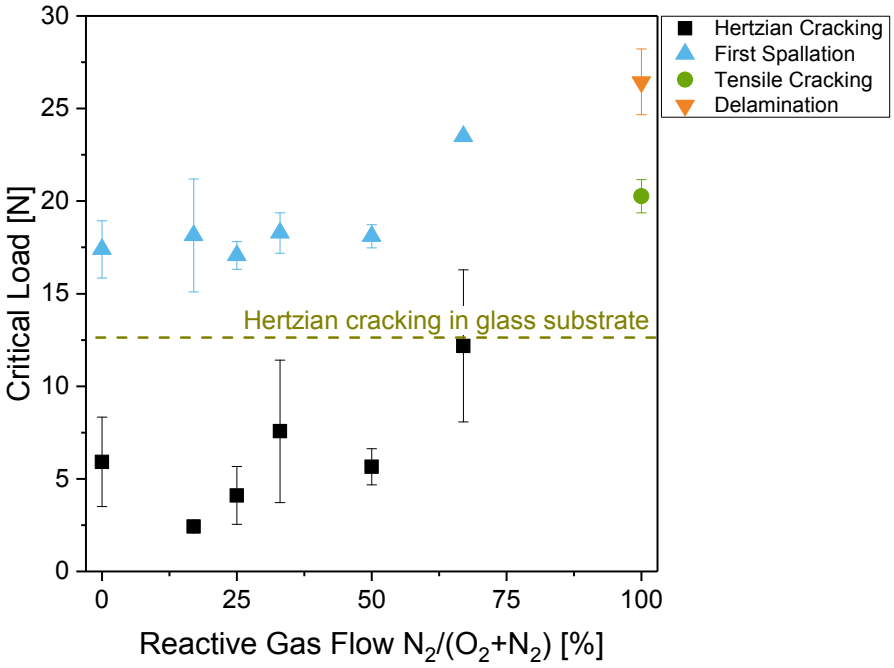

Figure 4.9: Critical loads obtained by scratch tests with a conical diamond indenter as a function of the gas flow $N_2/(O_2+N_2)$ ratio. The L_{C1} value obtained for the uncoated substrate is indicated by the dashed line.

the one grown at a gas flow $N_2/(O_2+N_2)$ ratio of 100 %, hence without O. For the Mo-O-N films with gas flow $N_2/(O_2+N_2)$ ratios up to 50 %, the Hertzian cracks first appeared at loads around 5 N, which is below the critical load for Hertzian cracking in the uncoated substrate. At higher loads of about 18 N, additionally recovery spallation occurred in the Mo-O-N films, which is caused by the elastic recovery behind the scratching tip [57–59]. For the Mo-O-N film grown at a gas flow $N_2/(O_2+N_2)$ ratio of 67 % both, the Hertzian cracking and recovery spallation are delayed to higher loads. Also the spallation is reduced compared to, e.g., the Mo-O-N film grown at a gas flow $N_2/(O_2+N_2)$ ratio of 50 %. Even though the elastic recovery of this film is higher compared to the Mo-O-N films with lower gas flow $N_2/(O_2+N_2)$ ratios, the H/E_r ratio increased as well, which indicates an increased resistance to cracking. Apart from recovery spallation the Mo-O-N films, except for the one grown without O, showed no extensive delamination.

The Mo-O-N film deposited without O on a Mo interlayer, however, exhibits different failure modes, such as tensile cracking and delamination from the substrate. These only occur at loads higher than 20 N. Due to the Mo interlayer and the crystalline structure, this is a different film system than the other Mo-O-N films and they are therefore not directly comparable. However, the same film deposited without an interlayer, gradually delaminated without an implemented load, and it was, therefore, not possible to find a

continuous area to perform scratch tests. Even with the deposition of an Mo interlayer, to reduce the constraint caused by the substrate, the film showed delamination at lower loads than the remaining films.

4.4 Optical Properties

Figure 4.10 visualises the optical appearance of the different films with 200 nm thickness deposited on glass and Si substrate. Already with the naked eye, there is an obvious change in transmittance and coloration visible, especially at gas flow $N_2/(O_2+N_2)$ ratios between 0 % and 50 %. The measured change in transmittance, absorbance and reflectance are depicted in Figure 4.11 for different compositions and thicknesses as a function of wavelength. When focusing on the transmittance spectra, it is obvious that with an increasing gas flow $N_2/(O_2+N_2)$ ratio the opacity increases and the appearance of the interference fringes, that are clearly visible for the 1000 nm thick transparent films, is less pronounced for higher gas flow $N_2/(O_2+N_2)$ ratios and lower film thicknesses. A change in thickness also seems to have an effect on the absorption band edge, i.e. the wavelength at which a transition from absorbing to transparent occurs within the material. Reducing the thickness from 1000 nm to 100 nm leads to a shift of approximately 75 nm towards lower wavelengths. In previous studies this phenomenon is explained by a lower carrier concentration at lower thicknesses [76]. Since this absorption band edge is still at a higher wavelength than for soda lime glass, the substrate has no influence on the optical properties of the Mo-O-N films.

The Mo-O-N films grown at low gas flow $N_2/(O_2+N_2)$ ratios show a high transmittance over the whole wavelength range investigated and the absorbance is, therefore, low. With increasing gas flow $N_2/(O_2+N_2)$ ratio, the transmittance decreases and the absorbance increases, while the reflectance is rather low for almost all Mo-O-N films. The Mo-O-N films grown at gas flow $N_2/(O_2+N_2)$ ratios of 50 % and 67 % show a high absorbance of 80-90 % over the entire measured wavelength range that naturally decreases with decreasing film thickness, since there is less material to interact with the light wave. The metal-like Mo-O-N film grown at a gas flow $N_2/(O_2+N_2)$ ratio of 100 % and the Mo film are in almost equal parts absorbing and reflecting, regardless of the wavelength and with no significant change with varying thickness. Except for the Mo-O-N film grown at a gas flow $N_2/(O_2+N_2)$ ratio of 100 %, the reflectance of the Mo-O-N films is below 30 % over the whole wavelength range investigated. Only the Mo-O-N film grown at a gas flow $N_2/(O_2+N_2)$ ratio of 67 % shows higher reflectance than 30 % at reduced film thickness as a result of the decreasing absorbance and only minimal change in transmittance.

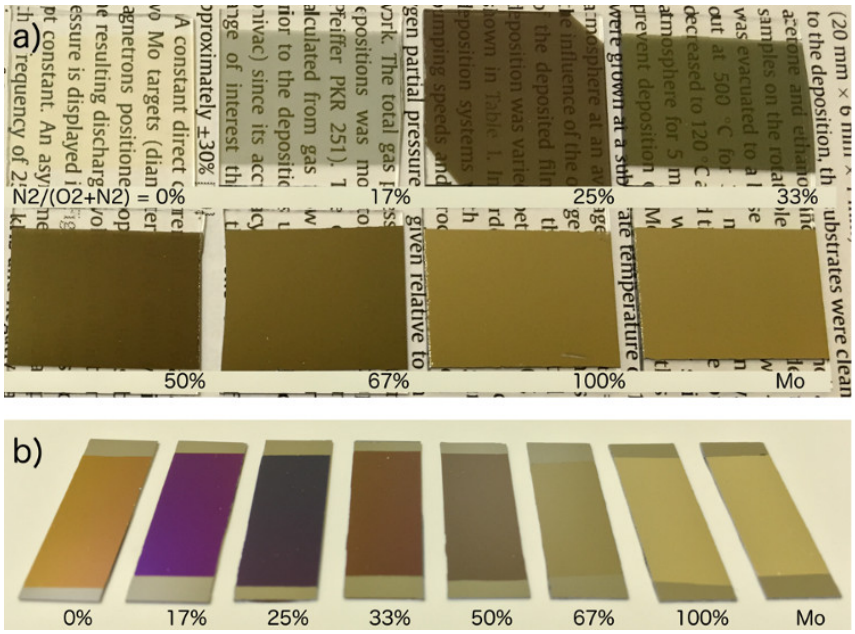

Figure 4.10: Visual appearance of Mo-O-N films and of Mo films grown on a) soda lime glass and b) silicon with a thickness of 200 nm. The percentage values indicate the gas flow $N_2/(O_2+N_2)$ ratios during deposition.

Figure 4.12 depicts the transmittance, absorbance and reflectance of all synthesised Mo-O-N films detected at 550 nm, as it is the wavelength most sensitive to the human eye [77]. This display shows more clearly that with increasing gas flow $N_2/(O_2+N_2)$ ratio there is a transition from a transparent via an absorbing to a reflecting material. Especially for a gas flow $N_2/(O_2+N_2)$ ratio below 50 %, where no N was detected with ERDA, there is a drastic decrease in transmittance. Ref. [17] also reported a similar transition as a result of an increasing Ar/O_2 gas flow ratio during deposition that resulted in the formation of lower oxidised MoO_x phases, which showed a lower transmittance than MoO_3 with the highest O content.

In Figure 4.12, there is also a noticeable influence displayed due to a change in film thickness, especially in the region, where the transition from a transparent to an opaque material occurs. The transition takes place at a reduced slope for thinner films with a film thickness of 100 nm than for thicker films with a thickness of 1000 nm. For Mo-O-N with a high N content, however, the thickness needs to be reduced significantly in order to enhance the transmittance. At a thickness of 40 nm, the Mo-O-N film grown at a gas flow $N_2/(O_2+N_2)$ ratio of 67 % still shows a transmittance below 20 %.

With increasing gas flow $N_2/(O_2+N_2)$ ratio during deposition, the absorption reaches its maximum value of about 90 % for the Mo-O-N film grown at a gas flow $N_2/(O_2+N_2)$ ratio of 50 %, while the reflectance shows a minimum for the Mo-O-N films grown at gas flow

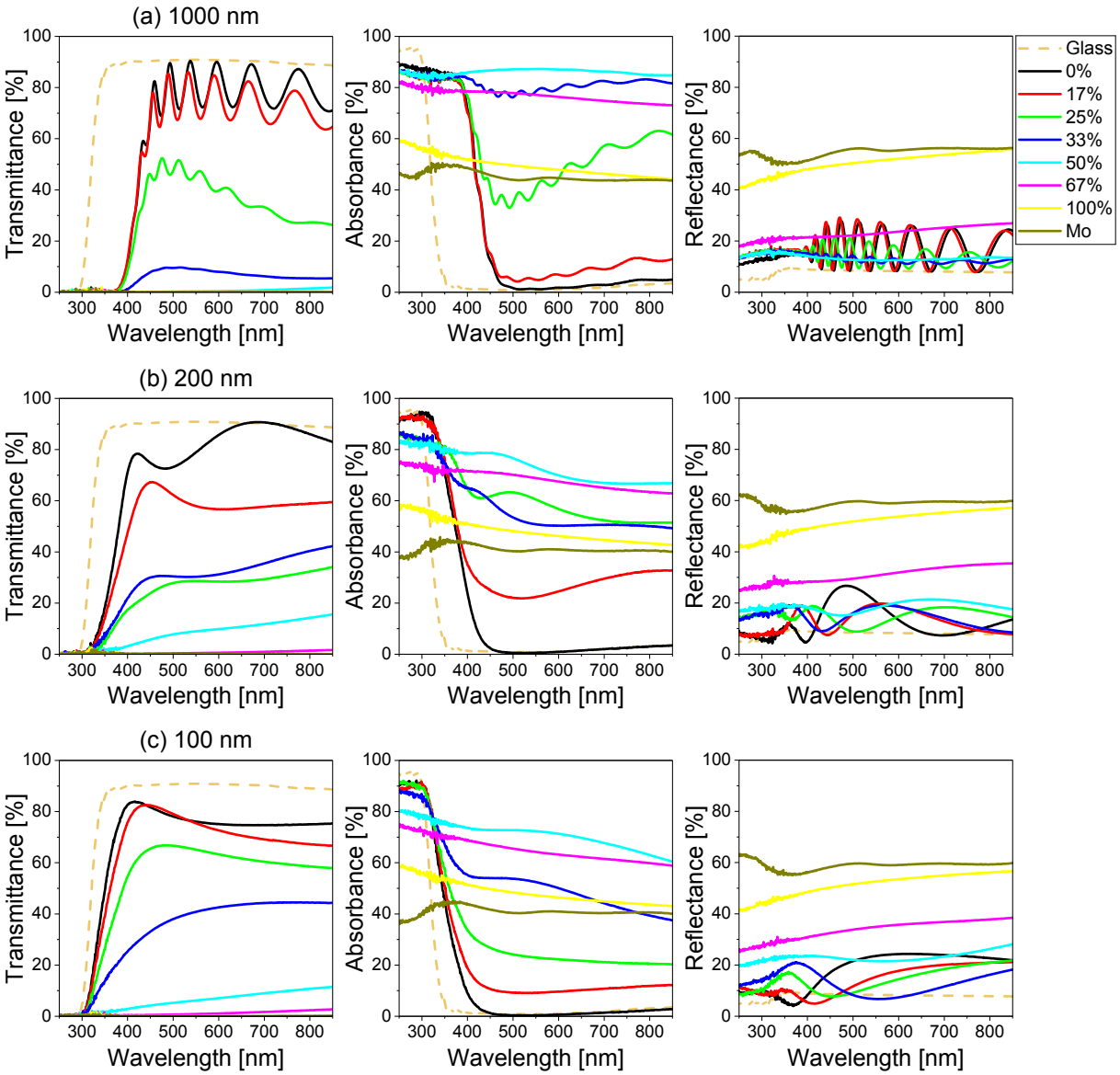

Figure 4.11: Transmittance, absorbance and reflectance of a) 1000 nm, b) 200 nm and c) 100 nm thick films grown at different gas flow $N_2/(O_2+N_2)$ ratios as a function of wavelength. The uncoated glass substrate and Mo films are added for reference.

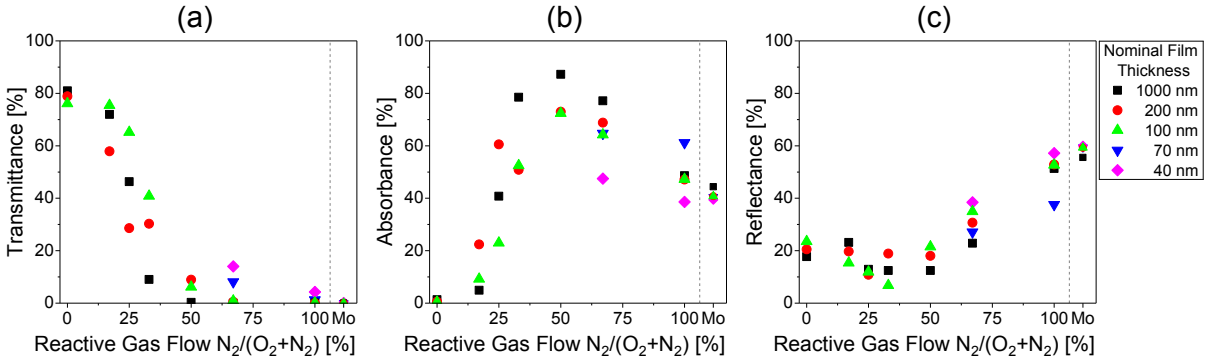

Figure 4.12: a) Transmittance, b) absorbance and c) reflectance determined at a wavelength of 550 nm of films grown at different gas flow $N_2/(O_2+N_2)$ ratios and of Mo films, that are separated by the dashed lines, for different thicknesses.

$N_2/(O_2+N_2)$ ratios between 25 % and 33 %. With further rise of the gas flow $N_2/(O_2+N_2)$ ratio, the absorbance decreases and the reflectance increases until the Mo-O-N film grown at a gas flow $N_2/(O_2+N_2)$ ratio of 100 % reaches almost the same levels of absorbance and reflectance as Mo. For the reflectance, there is no obvious trend due to the change in thickness observable. The occurring fluctuations possibly result from different surface conditions.

In addition to transmittance, reflectance and absorbance, also the refractive index and extinction coefficient as shown in Figure 4.13 were determined and the influence of composition and thickness of the Mo-O-N films was analysed. Both, the refractive index and extinction coefficient increase with increasing gas flow $N_2/(O_2+N_2)$ ratio. The refractive index of the Mo-O-N film grown at a gas flow $N_2/(O_2+N_2)$ ratio of 0 % is around 2.1 at a wavelength of 550 nm and the extinction coefficient is zero, which is characteristic for insulating materials [42]. All Mo-O-N films grown at gas flow $N_2/(O_2+N_2)$ ratios up to 33 % have a refractive index comparable to the Mo-O-N film grown without N addition with a decreasing tendency for lower film thicknesses, as a result of a reduced density [42]. However, at gas flow $N_2/(O_2+N_2)$ ratios greater than 50 % the refractive index increases and also the influence due to a reduced thickness is more pronounced. However, there the decreasing film thickness increases the refractive index. This behaviour was also observed in amorphous $Ge_{30}Se_{70}$ films, which is attributed to decreasing long-range disorder with decreasing film thickness [78].

In Figure 4.13 b) it is obvious that the extinction coefficient is already severely increasing at gas flow $N_2/(O_2+N_2)$ ratios lower than 50 %. Also the film thickness has a greater influence, for some films even to the extent of one magnitude when comparing 1000 nm to 100 nm thick films. A possible explanation is the formation of O vacancies due to the increased Ar/O_2 ratio in the first stage of deposition and with increasing gas flow

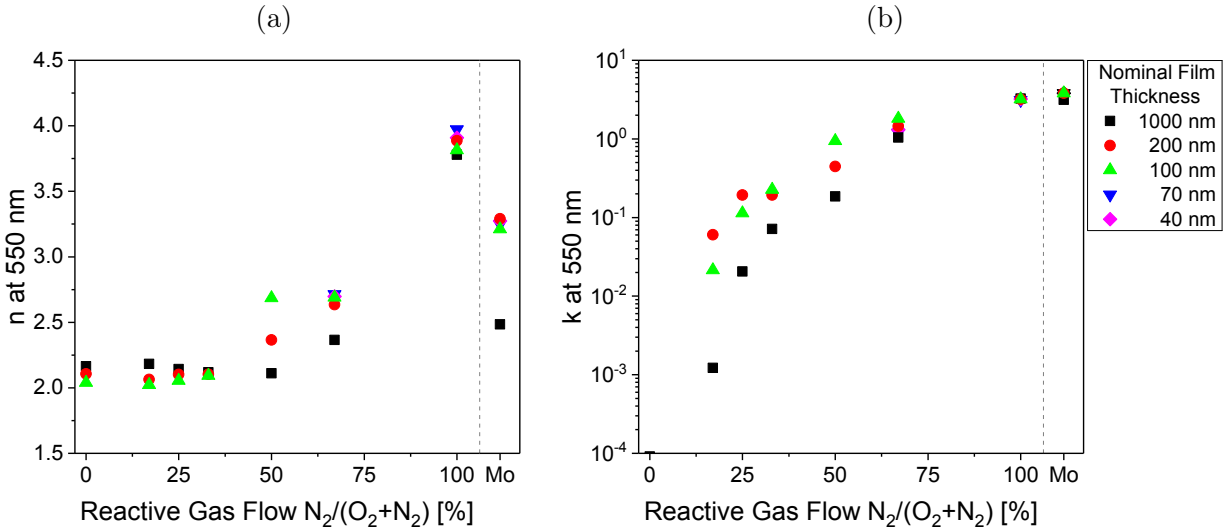

Figure 4.13: a) Refractive index n and b) extinction coefficient k determined at 550 nm for films with different thicknesses grown at different gas flow $N_2/(O_2+N_2)$ ratios and for Mo films that are separated by the dashed lines.

$N_2/(O_2+N_2)$ ratio.

For metallic and metal-like materials it is common that the values of the refractive index and the extinction coefficient are of similar magnitude [42]. This is also the case for the Mo-O-N film grown at a gas flow $N_2/(O_2+N_2)$ ratio of 100 % and for the Mo film. Except for the 1000 nm thick Mo film, a variation in film thickness does not have a pertinent influence on the values. The difference in refractive index of the 1000 nm thick Mo film is unreasonably high and at the current knowledge not explainable. The evolution of the extinction coefficient is in agreement with the decrease in transmittance of the Mo-O-N films with increasing gas flow $N_2/(O_2+N_2)$ ratios, since the extinction coefficient is directly proportional to the absorption coefficient. It is therefore also reasonable that the extinction coefficient of the transparent Mo-O-N film grown at a gas flow $N_2/(O_2+N_2)$ ratio of 0 % is very low.

4.5 Electrical Properties

By using the Tauc-Lorentz oscillator during SE analysis, it was possible to determine approximate values of the band gap energy of the different films, which are displayed in Figure 4.14. The values of the Mo-O-N films up to a gas flow $N_2/(O_2+N_2)$ ratio of 33 % vary between 2.4 eV and 3.2 eV for different thicknesses, but show a decreasing tendency with increasing gas flow $N_2/(O_2+N_2)$ ratios. This can again be attributed to a lower

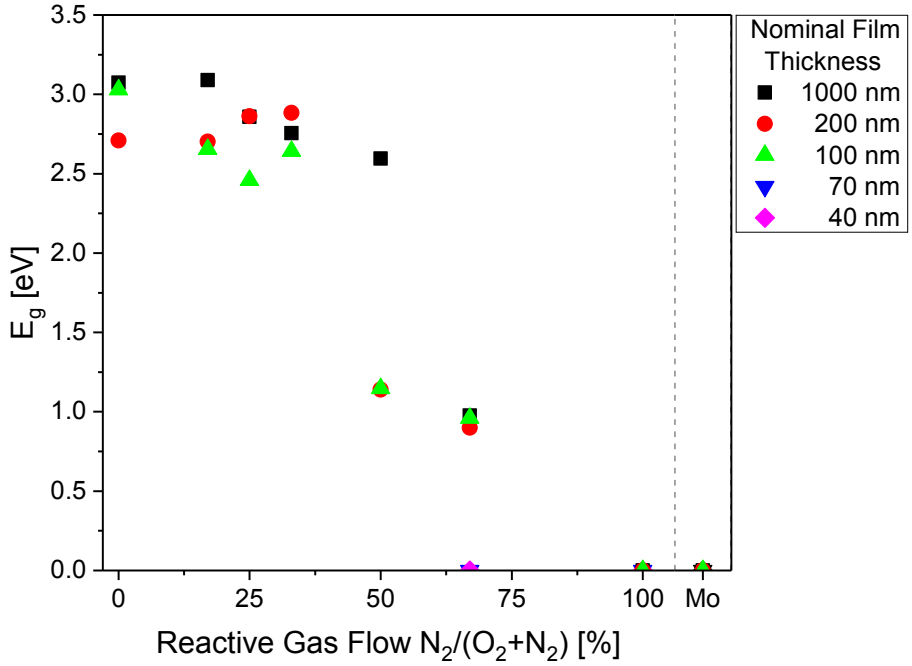

Figure 4.14: Band gap E_g obtained by SE of the Mo-O-N films grown at different gas flow $N_2/(O_2+N_2)$ ratios and of the Mo films (right).

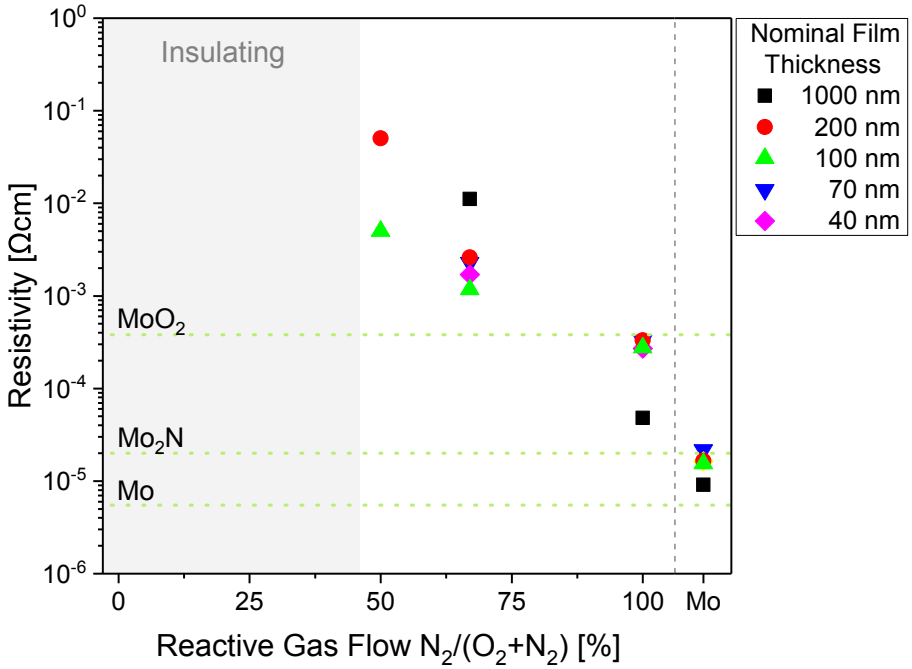

Figure 4.15: Electric resistivity of Mo films (right) and of Mo-O-N films grown at $N_2/(O_2+N_2)$ ratios of 0-100 % for different thicknesses. The dashed lines indicate reference values of the resistivity of MoO_2, Mo_2N and Mo from literature [24, 79].

oxidised MoO_x. For the Mo-O-N film grown at a gas flow $N_2/(O_2+N_2)$ ratio of 50 %, a strong reduction in E_g from 2.7 eV to 1 eV was observed due to the decrease in film thickness. In a similar way, the band gap energy gradually decreases to 0 eV upon further increase of the gas flow $N_2/(O_2+N_2)$ ratio.

The electrical resistivity of the films shown in Figure 4.15 corresponds well to the band gap energies detected by SE. For the Mo-O-N films with a high O content, i.e. deposition at gas flow $N_2/(O_2+N_2)$ ratios of 0 % to 33 % and E_g values greater than 2 eV, the measuring range limit of the four point probe was exceeded. These films were therefore marked as insulating. However, with increasing gas flow $N_2/(O_2+N_2)$ ratio the resistivity decreases towards the reference value for Mo_2N according to literature [24]. With reduced thicknesses, the resistivity increases for the Mo-O-N film grown at a gas flow $N_2/(O_2+N_2)$ ratio of 100 % and the Mo film as a result of increased surface scattering and lower carrier concentration [42, 76]. Yet, for the Mo-O-N films grown at gas flow $N_2/(O_2+N_2)$ ratios of 50 % and 67 %, a decrease in resistivity with decreasing thickness was observed. This might be caused by the formation of oxygen vacancies during the ignition sequence of the deposition. Even though the O_2 flow is reduced and there is a measurable N content in the Mo-O-N films grown at gas flow $N_2/(O_2+N_2)$ ratios of 50 % and 67 %, the O content is still dominating; hence, the increased Ar/O_2 ratio could still have a noticeable influence, especially for thinner films. This influence could, therefore, contribute as a decreased resistivity of a lower oxidised MoO_x compared to MoO_3. However, these are speculations and a definite explanation based on the results from the current work seems not feasible; further studies are necessary to clarify this effect.

5 Conclusions

Mo-O-N films with varying reactive $N_2/(O_2+N_2)$ gas flow ratios to modify the O/N ratio within the films and different thicknesses were deposited by DC reactive magnetron sputtering and the composition and microstructure as well as the mechanical, optical and electrical properties were investigated. In general, the synthesised films show mostly an amorphous structure, lower hardness and reduced modulus than a pure Mo film and sufficient adhesion on glass substrates, yet during scratch tests Hertzian cracking followed by recovery spallation at relatively low loads were noticed.

At low gas flow $N_2/(O_2+N_2)$ ratios up to 50 %, the transmittance is tuneable from transparent to absorbing, but all films show a high band gap energy of about 3 eV and, hence, high resistivity. Even though the N_2 flow rate is increasing in this region, no incorporation into the films was observed due to the higher reactivity of O than that of N. The changes in optical and electrical properties of the films are therefore a result of the increase in the Ar/O_2 ratio and the formation of O vacancies as less O is available during film growth. The influence of incorporated N is most prominent at a gas flow $N_2/(O_2+N_2)$ ratio of 50 % and higher. With increasing N content in the films, the oxidation states of Mo decrease and the films become crystalline. Their properties change towards a more metal-like behaviour; that means the refractive index and extinction coefficient increase, the band gap energy and resistivity decrease and the mechanical properties are improved.

The thickness of the Mo-O-N films also has an influence, especially, on the optical and electrical properties. As the film thickness was reduced, an increase in transmittance, refractive index and extinction coefficient was observed. Except for the metal-like Mo-O-N film without O and for the Mo film, where the resistivity is increasing with decreasing thickness due to enhanced scattering of electrons at grain boundaries, the Mo-O-N films show improved electrical conductivity at reduced film thicknesses. This is most likely associated to the plasma ignition sequence with the used higher Ar flow, which resulted in a thin interlayer with higher Mo content. The higher conductivity of this thin interlayer has a stronger influence on the electrical properties of the Mo-O-N films at lower thickness.

Overall, the obtained results correlated well with data reported in literature. Although the observed optical and electrical properties are still insufficient to use Mo-O-N as transparent conductive thin films, their high absorbance in the entire visible range enables their use as absorbing thin films. However, future research could be directed to produce even thinner Mo-O-N films to enable a sufficient level of transmittance or to enhance the conductivity of the transparent films with a more precise adjustment of the O/N ratio in the films or the introduction of a different dopant.

References

[1] R. Bel, H. Tahar, T. Ban, Y. Ohya, and Y. Takahashi, "Tin doped indium oxide thin films : Electrical properties," *Journal of Applied Physics*, vol. 2631, no. 1998, 2011.

[2] P. P. Edwards, A. Porch, M. O. Jones, D. V. Morgan, and R. M. Perks, "Basic materials physics of transparent conducting oxides," *Dalton Transactions*, no. 19, p. 2995, 2004.

[3] H. Hosono, "Recent progress in transparent oxide semiconductors: Materials and device application," *Thin Solid Films*, vol. 515, no. 15, pp. 6000–6014, 2007.

[4] D. Kim, Y. Han, J.-S. Cho, and S.-K. Koh, "Low temperature deposition of ITO thin films by ion beam sputtering," *Thin Solid Films*, vol. 377–378, pp. 81–86, 2000.

[5] Y. Leterrier, C. Fischer, L. Médico, F. Demarco, J.-A. E. Månson, P. Bouten, J. Degoede, and J. A. Nairn, "Mechanical properties of transparent functional thin films for flexible displays," *Coaters*, vol. 505, no. 1, pp. 856–7188, 2003.

[6] T. Minami, "Present status of transparent conducting oxide thin-film development for Indium-Tin-Oxide (ITO) substitutes," *Thin Solid Films*, vol. 516, no. 17, pp. 5822–5828, 2008.

[7] T. M. Barnes, M. O. Reese, J. D. Bergeson, B. A. Larsen, J. L. Blackburn, M. C. Beard, J. Bult, and J. Van De Lagemaat, "Comparing the fundamental physics and device performance of transparent, conductive nanostructured networks with conventional transparent conducting oxides," *Advanced Energy Materials*, vol. 2, no. 3, pp. 353–360, 2012.

[8] C. C. Yu, S. Ramanathan, and S. T. Oyama, "New Catalysts for Hydroprocessing : Bimetallic Oxynitrides M_I – M_{II} – O – N (M_I, M_{II} = Mo , W , V , Nb , Cr , Mn , and Co)," *Journal of Catalysis*, vol. 9, pp. 1–9, 1998.

[9] K. Stanczyk, H. S. Kim, C. Sayag, D. Brodzki, and G. Djega-Mariadassou, "HDN of 1–4 tetrahydroquinoline over MoNxOy and NbNxOy: effect of transition metal, solvent and ammonia," *Catalysis Letters*, vol. 53, no. 1/2, pp. 59–64, 1998.

[10] S. Venkataraj, D. Severin, S. H. Mohamed, J. Ngaruiya, O. Kappertz, and M. Wuttig, "Towards understanding the superior properties of transition metal oxynitrides prepared by reactive DC magnetron sputtering," *Thin Solid Films*, vol. 502, no. 1-2, pp. 228–234, 2006.

[11] A. Fuertes, "Syntheses and properties of functional oxynitrides - from photocatalysts to CMR materials," *Dalton Transactions*, vol. 39, no. 26, pp. 5942–5948, 2010.

[12] C. Pozo-Gonzalo, O. Kartachova, A. A. Torriero, P. C. Howlett, A. M. Glushenkov, D. M. Fabijanic, Y. Chen, S. Poissonnet, and M. Forsyth, "Nanoporous transition metal oxynitrides as catalysts for the oxygen reduction reaction," *Electrochimica Acta*, vol. 103, pp. 151–160, 2013.

[13] C. Gupta, *Extractive Metallurgy of Molybdenum*. Boca Raton, USA: CRC Press, 1992.

[14] N. Lepora, *Molybdenum*. Elements (Benchmark Books), New York, USA: Marshall Cavendish Benchmark, 2006.

[15] L. L. Chang and B. Phillips, "Phase relations in refractory metal-oxygen systems," *Journal of the American Ceramic Society*, vol. 52, no. 10, pp. 527–533, 1969.

[16] D. B. Rogers, R. D. Shannon, A. W. Sleight, and J. L. Gillson, "Crystal chemistry of metal dioxides with rutile-related structures," *Inorganic Chemistry*, vol. 8, no. 4, pp. 841–849, 1969.

[17] J. M. Pachlhofer, A. T. Martín-Luengo, R. Franz, E. Franzke, H. Köstenbauer, J. Winkler, A. Bonanni, and C. Mitterer, "Industrial-scale sputter deposition of molybdenum oxide thin films: Microstructure evolution and properties," *Journal of Vacuum Science and Technology A: Vacuum, Surfaces, and Films*, vol. 35, no. 2, p. 021504, 2017.

[18] J. M. Pachlhofer, C. Jachs, R. Franz, E. Franzke, H. Köstenbauer, J. Winkler, and C. Mitterer, "Structure evolution in reactively sputtered molybdenum oxide thin films," *Vacuum*, vol. 131, pp. 246–251, 2016.

[19] J. Scarminio, A. Lourenço, and A. Gorenstein, "Electrochromism and photochromism in amorphous molybdenum oxide films," *Thin Solid Films*, vol. 302, no. 1-2, pp. 66–70, 1997.

[20] T. He and J. Yao, "Photochromism of molybdenum oxide," *Journal of Photochemistry and Photobiology C: Photochemistry Reviews*, vol. 4, no. 2, pp. 125–143, 2003.

[21] Y. C. Tseng, A. U. Mane, J. W. Elam, and S. B. Darling, "Ultrathin molybdenum oxide anode buffer layer for organic photovoltaic cells formed using atomic layer deposition," *Solar Energy Materials and Solar Cells*, vol. 99, pp. 235–239, 2012.

[22] L. Cheng, M. Shao, X. Wang, and H. Hu, "Single-crystalline molybdenum triox-

ide nanoribbons: photocatalytic, photoconductive, and electrochemical properties," *Chemistry - A European Journal*, vol. 15, no. 10, pp. 2310–2316, 2009.

[23] D. Mutschall, K. Holzner, and E. Obermeier, "Sputtered molybdenum oxide thin films for NH_3 detection," *Sensors and Actuators B-Chemical*, vol. 36, no. 1-3, pp. 320–324, 1996.

[24] S. T. Oyama, *The Chemistry of Transition Metal Carbides and Nitrides*, ch. Introduction to the chemistry of transition metal carbides and nitrides, pp. 1–27. Dordrecht, Deutschland: Springer-Verlag, 1996.

[25] I. Jauberteau, A. Bessaudou, R. Mayet, J. Cornette, J. Jauberteau, P. Carles, and T. Merle-Méjean, "Molybdenum nitride films: Crystal structures, synthesis, mechanical, electrical and some other properties," *Coatings*, vol. 5, no. 4, pp. 656–687, 2015.

[26] D. A. Papaconstantopoulos, W. E. Pickett, B. M. Klein, and L. L. Boyer, "Electronic properties of transition-metal nitrides: The group-V and group-VI nitrides VN, NbN, TaN, CrN, MoN, and WN," *Physical Review B*, vol. 31, pp. 752–761, 1985.

[27] V. Anitha, A. Bhattacharya, N. G. Patil, and S. Major, "Study of sputtered molybdenum nitride as a diffusion barrier," *Thin Solid Films*, vol. 236, no. 1, pp. 306 – 310, 1993.

[28] Y. Wang, J. W. Seok, and R. Y. Lin, "Properties of molybdenum nitride thin film deposited by reactive sputter deposition," *Materials Research Society Proceedings*, vol. 750, no. 100, 2003.

[29] V. Anitha, S. Vitta, and S. Major, "Structure and properties of reactivity sputtered γ-Mo_2N hard coatings," *Thin Solid Films*, vol. 245, no. 1, pp. 1 – 3, 1994.

[30] J. Valli, U. Mäkelä, and H. T. G. Hentzell, "Tribological properties of MoN_x coatings in contact with copper," *Journal of Vacuum Science & Technology A*, vol. 4, no. 6, pp. 2850–2854, 1986.

[31] A. Srifa, K. Okura, T. Okanishi, H. Muroyama, T. Matsui, and K. Eguchi, "CO_x-free hydrogen production via ammonia decomposition over molybdenum nitride-based catalysts," *Catalysis Science and Technology*, vol. 6, no. 20, pp. 7495–7504, 2016.

[32] H. Ihara, M. Hirabayashi, K. Senzaki, Y. Kimura, and H. Kezuka, "Superconductivity of B1-MoN films annealed under high pressure," *Physical Review B*, vol. 32, pp. 1816–1817, 1985.

[33] K. Kawaguchi and S. Shin, "Structural and superconducting properties of artificially

superstructured MoN-TiN films," *Journal of Applied Physics*, vol. 67, no. 2, pp. 921–929, 1990.

[34] Y. Sutou, S. Komiyama, M. Sonobe, D. Ando, J. Koike, and M. Wang, "Microstructure, hardness and wear resistance of reactive sputtered Mo-O-N films on stainless steel substrate," *Surface and Coatings Technology*, vol. 280, pp. 1–7, 2015.

[35] R. Asahi, T. Morikawa, T. Ohwaki, K. Aoki, and Y. Taga, "Visible-light photocatalysis in nitrogen-doped titanium oxides," *Science*, vol. 293, no. 5528, pp. 269–271, 2001.

[36] T. Bécue, J.-M. Manoli, C. Potvin, and G. Djéga-Mariadassou, "Preparation, characterization, and catalytic behavior of molybdenum oxynitrides supported on EMT zeolite (NaEMT and HEMT) catalysts," *Journal of Catalysis*, vol. 170, no. 1, pp. 123–131, 1997.

[37] W. Ji, R. Shen, R. Yang, G. Yu, X. Guo, L. Peng, and W. Ding, "Partially nitrided molybdenum trioxide with promoted performance as an anode material for lithium-ion batteries," *Journal of Materials Chemistry A*, vol. 2, no. 3, pp. 699–704, 2014.

[38] Y. G. Shen and Y.-W. Mai, "Reactively sputter-deposited Mo-O_x-N_y thin films," *Materials Science and Engineering*, vol. 95, pp. 222–229, 2002.

[39] J. A. Drayton, D. D. Williams, R. M. Geisthardt, C. L. Cramer, J. D. Williams, and J. R. Sites, "Molybdenum oxide and molybdenum oxide-nitride back contacts for CdTe solar cells," *Journal of Vacuum Science and Technology A: Vacuum, Surfaces, and Films*, vol. 33, no. 4, p. 041201, 2015.

[40] D. Depla, S. Mahieu, and J. E. Greene, *Sputter Deposition Processes*. Oxford, UK: Elsevier Ltd., 3rd ed., 2010.

[41] D. M. Mattox, "Physical vapor deposition (PVD) processes," *Metal Finishing*, vol. 93, no. 1, pp. 394–408, 1995.

[42] M. Ohring, *The Materials Science of Thin Films*. San Diego, USA: Academic Press, 1992.

[43] J. A. Thornton and J. E. Greene, *Handbook of Deposition Technologies for Films and Coatings*, ch. Sputter Deposition Processes, pp. 275–345. Park Ridge, New Jersey, USA: Noyes Publications, 2nd ed., 1994.

[44] W. D. Sproul, "Multi-cathode unbalanced magnetron sputtering systems," *Surface and Coatings Technology*, vol. 49, no. 1-3, pp. 284–289, 1991.

[45] V. Linss, "Challenges in the industrial deposition of transparent conductive oxide materials by reactive magnetron sputtering from rotatable targets," *Thin Solid Films*, vol. 634, pp. 149–154, 2017.

[46] J. A. Thornton, "The microstructure of sputter-deposited coatings," *Journal of Vacuum Science and Technology A: Vacuum, Surfaces, and Films*, vol. 4, no. 6, pp. 3059–3065, 1986.

[47] J. A. Thornton, "High rate thick film growth," *Annual Review of Materials Science*, vol. 239, no. 60, pp. 239–260, 1977.

[48] I. Petrov, P. B. Barna, L. Hultman, and J. E. Greene, "Microstructural evolution during film growth," *Journal of Vacuum Science and Technology A: Vacuum, Surfaces, and Films*, vol. 21, no. 5, pp. 117–128, 2003.

[49] P. Barna and M. Adamik, "Fundamental structure forming phenomena of polycrystalline films and the structure zone models," *Thin Solid Films*, vol. 317, no. 1-2, pp. 27–33, 1998.

[50] B. Movchan and A. Demchishin, "Structure and properties of thick condensates of nickel, titanium, tungsten, aluminum oxides, and zirconium dioxide in vacuum," *Fizika Metallov i Metallovedenie*, vol. 28, pp. 653–660, 1969.

[51] R. Messier, A. P. Giri, and R. A. Roy, "Revised structure zone model for thin film physical structure," *Journal of Vacuum Science and Technology A: Vacuum, Surfaces, and Films*, vol. 2, no. 2, pp. 500–503, 1984.

[52] R. D. Bland, G. J. Kominiak, and D. M. Mattox, "Effect of ion bombardment during deposition on thick metal and ceramic deposits," *Journal of Vacuum Science and Technology*, vol. 11, no. 4, pp. 671–674, 1974.

[53] N. Kaiser, "Review of the fundamentals of thin-film growth," *Applied Optics*, vol. 41, no. 16, p. 3053, 2002.

[54] O. Kraft and C. Volkert, "Mechanical testing of thin films and small structures," *Advanced Engineering Materials*, vol. 3, no. 3, pp. 99–110, 2001.

[55] R. King, "Elastic analysis of some punch problems for a layered medium," *International Journal of Solids and Structures*, vol. 23, no. 12, pp. 1657 – 1664, 1987.

[56] A. Leyland and A. Matthews, "On the significance of the H/E ratio in wear control: A nanocomposite coating approach to optimised tribological behaviour," *Wear*, vol. 246, no. 1-2, pp. 1–11, 2000.

[57] Organization Technical Barriers to Trade (TBT) Committee., "Standard test method for adhesion strength and mechanical failure modes of ceramic coatings by quantitative single point scratch testing," *ASTM International*, vol. 05, no. Reapproved 2015, pp. 1–29, 2015.

[58] S. J. Bull, "Failure mode maps in the thin film scratch adhesion test," *Tribology International*, vol. 30, no. 7, pp. 491–498, 1997.

[59] P. Burnett and D. Rickerby, "The relationship between hardness and scratch adhesion," *Thin Solid Films*, vol. 154, no. 1, pp. 403 – 416, 1987.

[60] P. Steinmann, Y. Tardy, and H. Hintermann, "Adhesion testing by the scratch test method: The influence of intrinsic and extrinsic parameters on the critical load," *Thin Solid Films*, vol. 154, no. 1, pp. 333 – 349, 1987.

[61] R. E. Hummel, *Electronic Properties of Materials*. New York, USA: Springer-Verlag, 3rd ed., 2001.

[62] H. Fujiwara, *Spectroscopic Ellipsometry: Principles and Applications*. West Sussex, England: Wiley, 2007.

[63] M. Gilliot, "Extraction of complex refractive index of absorbing films from ellipsometry measurement," *Thin Solid Films*, vol. 520, no. 17, pp. 5568–5574, 2012.

[64] J. A. Woollam, B. Johs, C. M. Herzinger, J. N. Hilfiker, R. Synowicki, and C. L. Bungay, "Overview of variable angle spectroscopic ellipsometry (VASE), part I: Basic theory and typical applications," *Critical Reviews*, vol. 72, pp. 3–28, 1999.

[65] C. M. Herzinger, B. Johs, W. A. McGahan, J. A. Woollam, and W. Paulson, "Ellipsometric determination of optical constants for silicon and thermally grown silicon dioxide via a multi-sample, multi-wavelength, multi-angle investigation," *Journal of Applied Physics*, vol. 83, no. 6, pp. 3323–3336, 1998.

[66] I. Miccoli, F. Edler, H. Pfnür, and C. Tegenkamp, "The 100th anniversary of the four-point probe technique: The role of probe geometries in isotropic and anisotropic systems," *Journal of Physics Condensed Matter*, vol. 27, no. 22, 2015.

[67] L. B. Valdes, "Resistivity measurements on germanium for transistors," *Proceedings of the I-R-E*, vol. 29, pp. 420–427, 1952.

[68] F. M. Smits, "Measurement of sheet resistivities with the four-point probe," *Bell System Technical Journal*, vol. 37, no. 3, pp. 711–718, 1958.

[69] K. K. Shih and D. B. Dove, "Properties of W–N and Mo–N films prepared by reactive

sputtering," *Journal of Vacuum Science and Technology A: Vacuum, Surfaces, and Films*, vol. 8, no. 3, pp. 1359–1363, 1990.

[70] A. Fan, L. Qin, L. Tian, and B. Tang, "Corrosion resistance of molybdenum nitride modified Ti_6Al_4V alloy in HCl solution," *Journal Wuhan University of Technology, Materials Science Edition*, vol. 23, no. 3, pp. 358–361, 2008.

[71] P. F. Carcia and E. M. McCarron, "Synthesis and properties of thin film polymorphs of molybdenum trioxide," *Thin Solid Films*, vol. 155, no. 1, pp. 53–63, 1987.

[72] G. Linker, R. Smithey, and O. Meyer, "Superconductivity in MoN films with NaCl structure," *Journal of Physics F: Metal Physics*, vol. 14, no. 7, p. L115, 1984.

[73] A. Perry, A. Baouchi, J. Petersen, and S. Pozder, "Crystal structure of molybdenum nitride films made by reactive cathodic arc evaporation," *Surface and Coatings Technology*, vol. 54-55, pp. 261 – 265, 1992.

[74] J. Barbosa, L. Cunha, L. Rebouta, C. Moura, F. Vaz, S. Carvalho, E. Alves, E. Le Bourhis, P. Goudeau, and J. P. Rivière, "Properties of MoN_xO_y thin films as a function of the N/O ratio," *Thin Solid Films*, vol. 494, no. 1-2, pp. 201–206, 2006.

[75] S. S. Bhat, U. V. Waghmare, and U. Ramamurty, "Effect of oxygen vacancies on the elastic properties of zinc oxide: A first-principles investigation," *Computational Materials Science*, vol. 99, pp. 133 – 137, 2015.

[76] S. Rahmane, M. S. Aida, M. A. Djouadi, and N. Barreau, "Effects of thickness variation on properties of ZnO:Al thin films grown by RF magnetron sputtering deposition," *Superlattices and Microstructures*, vol. 79, pp. 148–155, 2015.

[77] J. Chen, W. Cranton, and M. Fihn, *Handbook of visual display technology*. New York, USA: Springer-Verlag, 2012.

[78] A. S. Solieman, M. M. Hafiz, A.-H. A. Abu-Sehly, and A.-N. A. Alfaqeer, "Dependence of optical properties on the thickness of amorphous $Ge_{30}Se_{70}$ thin films," *Journal of Taibah University for Science*, vol. 8, no. 3, pp. 282–288, 2014.

[79] H. Gruber and E. Krautz, "Untersuchungen der elektrischen Leitfähigkeit und des Magnetowiderstandes im System Molybdän-Sauerstoff," *Physica Status Solidi A*, vol. 62, pp. 615–624, 12 1980.